



Epitaxial TiC_x(001) layers: Phase formation and physical properties vs C-to-Ti ratio



Peijiao Fang^a, C.P. Mulligan^b, Ru Jia^a, Jian Shi^a, S.V. Khare^c, Daniel Gall^{a,*}

^a Department of Materials Science and Engineering, Rensselaer Polytechnic Institute, Troy, NY 12180, United States

^b U.S. Army Combat Capabilities Development Command, Armaments Center, Benét Laboratories, Watervliet, NY 12189, United States

^c Department of Physics and Astronomy, University of Toledo, Toledo, OH 43606, United States

ARTICLE INFO

Article history:

Received 28 October 2021

Revised 23 December 2021

Accepted 10 January 2022

Available online 11 January 2022

Keywords:

Titanium carbide

Phase stability

Hardness

Electrical resistivity

Epitaxy

ABSTRACT

Titanium carbide films are deposited onto MgO(001) by reactive magnetron sputtering in Ar/CH₄ mixtures at 1100 °C with a varying CH₄ fraction $f_{\text{CH}_4} = 0.4\text{--}8\%$, yielding C-to-Ti ratios $x = 0.08\text{--}1.8$. The microstructure is dominated by an epitaxial rock-salt structure TiC_x(001) matrix which contains secondary hcp Ti and graphitic/a-C:H for $x \leq 0.24$ and $x \geq 1.5$, respectively. First-principles calculations indicate negligible interstitial C in the cubic phase, a large equilibrium phase-field $x = 0.5\text{--}1$ for the cubic structure which is extended to $x < 0.5$ by entropic stabilization, and a predicted C-solubility in hcp Ti of $x = 0.06$ at 1100 °C. The measured relaxed lattice constant increases from $a_0 = 0.4304$ nm for TiC_{0.5} to 0.4325 nm for TiC_{1.0}, in excellent agreement with predictions. However, da_0/dx for $x < 0.5$ and $x > 1.0$ is much smaller than predicted for C vacancies and interstitials in rock-salt TiC_x, respectively, confirming secondary phase formation and indicating a minimum $x = 0.46$ in the cubic phase. The hardness and elastic modulus of phase-pure TiC_x(001) increases from $H = 24$ GPa and $E = 304$ GPa for TiC_{0.5} to $H = 31$ GPa and $E = 462$ GPa for TiC_{1.0}, which is attributed to an increasing bonding ionicity. H and E decrease with $x < 0.5$ and $x > 1.0$ due to secondary phase softening which is well described by an effective medium with homogenous stress. The electrical resistivities for TiC_{0.5} and TiC_{1.0} are 168 and 83 $\mu\Omega$ cm at 298 K, and 158 and 72 $\mu\Omega$ cm at 77 K, indicating electron scattering at random anion vacancies for $x = 0.5$ but also dominant defect scattering for stoichiometric TiC_{1.0}.

© 2022 Acta Materialia Inc. Published by Elsevier Ltd. All rights reserved.

1. Introduction

Transition metal carbides are of broad interest due to their thermal stability, chemical inertness, metallic conductivity, high hardness and wear resistance [1–8]. Titanium carbide is the most studied early transition metal carbide. It possesses a good electrical and thermal conductivity, a high hardness and low friction coefficient [9–11], and is attractive for a wide range of applications including as protective hard coating [9,12], as low-resistivity ohmic contact to SiC [13], as seed layer for growth of Ti-based MAX phase materials and graphene layers [14–16], and as transparent conductive 2D MXene Ti₃C₂ in electronic, photonic and sensing applications [17]. The TiC mechanical properties including its wear resistance and resistance against plastic deformation have been intentionally tailored by controlling its nanostructure and its incorporation into nanocomposite, multilayer, or superlattice coatings [10,18–26]. However, reported values for the hardness H and elastic modulus

E of TiC_x vary widely and no consensus on the intrinsic TiC properties has emerged yet. More specifically, ion-implanted nanocrystalline TiC_x films show an increasing $H = 24\text{--}35$ GPa and $E = 265\text{--}386$ GPa with increasing $x = 0.49\text{--}0.78$ [10]; titanium carbide layers grown by plasma-enhanced chemical vapor deposition have an average $H = 22$ GPa and $E = 268$ GPa [21]; sputter-deposited 111-textured cubic TiC_x layers exhibit a maximum $H = 26$ GPa when x reaches 0.5 [27], but a wide range of $H = 5.5\text{--}35$ GPa and $E = 61\text{--}340$ GPa have been reported for sputter-deposited TiC/a-C(:H) nanocomposites where the C-to-Ti ratio x controls the Ti and/or free carbon volumetric fraction, the grain size, and the bonding in the amorphous carbon phase [22,25,26,28,29]. That is, the TiC_x mechanical properties vary strongly as a function of synthesis method which, in turn, affect its composition and microstructure, resulting in a large uncertainty in the intrinsic properties. We envision that epitaxial TiC_x layers can eliminate some of this uncertainty as their mechanical properties are measured in the absence of microstructural features including grain boundaries, secondary C-phases, and texture, yielding valuable data on the intrinsic properties of TiC. This approach of using epitaxial layers to measure intrinsic physical properties has been successfully em-

* Corresponding author.

E-mail address: galld@rpi.edu (D. Gall).

ployed to study intrinsic electrical, optical, and mechanical properties of many early transition metal nitrides [30–45]. In contrast, studies on the physical properties of epitaxial carbides are rare.

Titanium carbide crystallizes in a rock salt structure and exhibits a very wide reported homogeneity range from $\text{TiC}_{0.48}$ to $\text{TiC}_{1.00}$ [46] which is attributed to C vacancies. The two polymorphs of metallic Ti, hcp α -Ti and bcc β -Ti (> 920 °C), have a reported carbon solubility of 1.6% and 0.6%, respectively, above which phase separation to metallic Ti and TiC is expected [47]. Epitaxial growth of NaCl-structure TiC has been reported using chemical vapor deposition [48], physical vapor deposition [14,15,49–56], and chemical solution deposition [57]. This includes TiC(001) growth on MgO(001) from evaporated Ti and C_{60} at 400–500 °C [51], reactive sputter-deposition of TiC(001) on Si(001) in an Ar/acetylene mixture at 600 °C [49], TiC(111) seed layer deposition on MgO(111) and Al_2O_3 (0001) for subsequent MAX phase growth using Ti sputtering and C_{60} co-evaporation [14,15], reactive sputter deposition of TiC(001) in Ar/ CH_4 mixtures at 100–800 °C [53,54] or with high-power impulse magnetron sputtering at 200–800 °C [52]. These studies provide no details into the mechanical properties of epitaxial TiC_x , with the exception of Ref. [57] which indicates a hardness $H = 21$ GPa for $\text{TiC}_{1.1}$, however, measured with a 30–50 nm indentation depth for a 100 nm layer thickness. This motivates our study on the mechanical properties of phase pure epitaxial TiC_x , providing hardness and elastic modulus values in the absence of grain boundaries and secondary phases, but also on epitaxial TiC_x (001) with hcp Ti or a-C:H inclusions, to quantify the effect of secondary phases. In addition, we note that the electrical resistivity of epitaxial TiC_x has already been reported several times, but that the values vary widely from 110 to 620 $\mu\Omega$ cm [15,49,51–55,57], suggesting that crystalline defects strongly affect electron transport in TiC_x . This motivates the study of electron transport in TiC_x as a function of x using epitaxial layers with a particularly high crystalline quality, as facilitated in our investigation by a high deposition temperature of 1100 °C. The latter also serves to explore metastable phase formation and solubility limits at high temperature.

In this paper, we report the measured hardness, elastic modulus, electrical resistivity and lattice constants of epitaxial TiC_x layers as a function of the C-to-Ti ratio x , and explore phase stability and solubility limits using first-principles calculations. TiC_x layers with varying compositions of $x = 0.08$ –1.8 are grown by reactive DC magnetron sputtering on single crystal MgO(001) substrates in Ar/ CH_4 gas mixtures. Structural analyses confirm that TiC_x grows epitaxially on the MgO substrates with a cube-on-cube relationship with $(001)_{\text{TiC}} \parallel (001)_{\text{MgO}}$ and $[100]_{\text{TiC}} \parallel [100]_{\text{MgO}}$ for $x = 0.8$ –1.5. Single-phase layers form for $x = 0.5$ –1.0 but $x \leq 0.24$ and $x \geq 1.5$ leads to secondary phase hcp Ti and graphitic/a-C:H inclusions, respectively. The experimental phases and lattice constants are in good agreement with first-principles calculations, including finite temperature entropic corrections. The hardness and elastic modulus are largest for single-phase layers with $x = 0.5$ –1.0, and decrease for $x < 0.5$ and $x > 1.0$ due to secondary phase inclusions. The resistivity vs composition exhibits a minimum for stoichiometric $\text{TiC}_{1.0}$, indicating an excellent crystalline quality and a minimum in defect scattering associated with random distribution of C-vacancies on anion sites.

2. Procedure

Titanium carbide layers were deposited in a three chamber ultra-high vacuum DC magnetron sputtering system with a base pressure of 10^{-9} Torr [58,59]. Single-side polished $10 \times 10 \times 0.5$ mm³ single crystal MgO(001) substrates were cleaned in sequential ultrasonic baths of trichloroethylene, acetone, isopropyl alcohol, and de-ionized water for 15 min each, blown

dry with nitrogen, mounted onto a Mo holder using colloidal silver paint, and inserted into the deposition system via a load lock chamber. The substrates were degassed in vacuum at 1100 °C for 1 h, using a radiative pyrolytic graphite heater. Depositions were performed at the same temperature, which was measured by a thermocouple below the substrate holder. 99.999% pure Ar, which was further purified with a MicroTorr purifier, and 99.999% pure CH_4 were introduced into the deposition chamber through needle valves to reach a constant total pressure of 5 mTorr with a CH_4 fraction f_{CH_4} which was varied from 0.4% to 8% to obtain samples with different C content. A 5 cm-diameter 0.6 cm-thick 99.99% pure Ti target was positioned 9 cm from the stage at a 45° tilt and was sputter cleaned for 10 min prior to each deposition with a shutter shielding the substrate. The stage was continuously rotated at 60 rpm to improve thickness uniformity and a constant power of 100 W was applied to the Ti target for a total deposition time of 2 h. The deposition rate decreases monotonically with increasing f_{CH_4} from 11 to 7 nm/min for $f_{\text{CH}_4} = 0.4\%$ –4% and increases slightly to 9 nm/min for higher $f_{\text{CH}_4} = 6$ –8%, as determined from film thickness measurements by cross-sectional scanning electron microscopy (SEM) indicating thicknesses of 900–1350 nm. The deposition rate was confirmed with a 5 min deposition at $f_{\text{CH}_4} = 4\%$ that yields a thickness of 36.3 nm as measured by x-ray reflectivity (XRR), corresponding to a rate of 7.26 nm/min which is in good agreement with 7.5 nm/min from the SEM measurement of the thick layer.

X-ray diffraction (XRD) scans were done in a Panalytical X'Pert PRO MPD system with a Cu $K\alpha$ ($\lambda = 1.5418$ Å) source with a 45 kV accelerating voltage and a 40 mA current. A Bragg-Brentano divergent beam geometry was used to collect θ – 2θ patterns over a large $2\theta = 5$ –85° range, to detect small inclusions of possible secondary phases or misoriented grains. ω rocking curves were acquired with a parallel beam geometry at a constant 2θ angle corresponding to the TiC 002 reflection, using a hybrid mirror with a two-bounce two-crystal Ge(220) monochromator, yielding a parallel incident beam with a wavelength $\lambda_{K\alpha 1} = 1.5406$ Å and a divergence of 0.0068°, and a PIXcel solid-state line detector operated in receiving mode with a 0.165 mm active length in combination with a 0.04 rad Soller slit, effectively acting as a point detector. Direct beam alignment, sample height adjustment, as well as correction of the substrate ω and χ tilt angles were performed prior to all scans. ϕ -scans were acquired at constant 2θ angles and χ tilts to detect TiC 113 and MgO 113 reflections, using a point source in combination with an x-ray lens yielding a quasi-parallel beam with an equatorial and axial divergence of 0.3°. Reciprocal space mapping (RSM) around 113 reflections were done using the hybrid mirror and taking advantage of all 256 channels of the solid-state line detector, using a small diffracted beam exit angle $\sim 10^\circ$ with respect to the sample surface to cause beam narrowing which increases the 2θ resolution.

X-ray photoelectron spectroscopy (XPS) was performed using Al $K\alpha$ radiation (1486.6 eV) in a PHI 5000 Versaprobe™ system with a hemispherical capacitor analyzer and a multichannel detector. Titanium carbide samples were sputter cleaned using 2 keV Ar^+ ions for 16 min prior to each acquisition. High-resolution spectra were collected for Ti 2p and C 1s peaks using a 23.5 eV pass energy, a 0.2 eV energy step and a 20 eV energy range. The C-to-Ti ratio was determined from the relative intensities of the area under the Ti 2p and C 1s peaks employing atomic sensitivity factors [60]. We note that the sputter cleaning may cause preferential sputtering and therefore a C-to-Ti surface composition that deviates from bulk. However, as presented in Section 3, the composition measured by XPS is in good agreement with Energy-dispersive X-ray spectroscopy (EDS) analyses, suggesting that selective sputtering has a negligible effect on the composition measurements. The EDS measurements were done in a FEI Helios Nanolab SEM operated

with a 5.0 kV accelerating voltage and a 5.0 mm working distance. An Oxford Instruments X-Max^N 80 silicon drift detector that is particularly well suited for light element detection was used to obtain the spectra. They were analyzed with the Oxford Instruments AZtec EDS software. We expect the measured accuracy of the C-to-Ti ratio to be $\pm 6\%$ for the TiC_x specimens, based on test measurements on a SiC standard using the same detector. No impurities other than surface contamination were detected by either XPS or EDS, suggesting an impurity concentration < 1 at.% in all layers, excluding the possible incorporation of hydrogen in the amorphous phase for large x , as discussed in Section 3. Room-temperature Raman spectra were collected using a WITec Alpha 300 confocal Raman microscope with a 500 μ W continuous-wave laser with a 532 nm wavelength, a 100 \times objective lens, a 7 μ m² spot size, and a T1 grating with an 1800 g/mm groove density and a 500 nm blaze wavelength.

Nanoindentation measurements were done using a Hysitron T1900 Triboindenter system with a diamond Berkovich tip with a three-sided pyramidal shape and a 100 nm radius. The tip area function of the Berkovich tip was carefully calibrated using a fused silica standard [61]. *In situ* scanning probe microscopy (SPM) imaging was performed before and after indentations using the same tip in contact mode with a setpoint of 2 μ N to determine the surface morphology and circumvent indentation at pre-existing surface cracks caused by sample cleavage. A set of twelve indents with increasing maximum displacements from 10 to 120 nm (in 10 nm steps) were performed on a 3 \times 4 position grid. Three such indentation sets were done at different sample locations for a total of 36 indentation experiments for each TiC_x sample. The contact depth h_c was $< 10\%$ of the film thickness for all indentations, rendering substrate effects negligible. The hardness and elastic moduli were determined using the Oliver and Pharr method [61]. All data points were included in the data analyses with the exception of a few ($< 15\%$) outliers with contact depths $h_c < 10$ nm (and maximum displacement ≤ 20 nm) that show particularly low hardness due to a not fully developed plastic zone [62]. In addition, six indents with maximum displacements $h_m = 40$ –140 nm (in 20 nm steps) were performed primarily to collect SPM micrographs of the indentations. The hardness H was determined from its definition $H = P_{\max} / A$, and the reduced modulus E_r from the upper portion of the unloading curve using $S = dP / dh = 2 E_r \sqrt{A} / \sqrt{\pi}$ [61] where P_{\max} , A , S , P , and h represent the maximum load, the projected contact area, stiffness, experimental load and displacement, respectively. The elastic modulus E of the TiC_x films are determined from the measured reduced modulus E_r using the expression $1/E_r = (1 - \nu^2) / E + (1 - \nu_i^2) / E_i$, where $E_i = 1141$ GPa and $\nu_i = 0.07$ are the Young's modulus and Poisson's ratio of the diamond tip [63], and $\nu = 0.21$ is the Poisson's ratio of the TiC_x films from Ref. [64]. We note that using a different value for ν , e.g. $\nu = 0.17$ from Ref. [65], introduces a negligible correction of 7 GPa to the determined E .

The sheet resistance was measured with a linear four-point-probe with spring loaded tips and a 1.0 mm inter-probe spacing. Measurements at 77 K were taken with the same linear four-point probe with both sample and probe tips completely immersed in liquid nitrogen. The measured sheet resistance was independent of the applied current of 1–5 mA for all samples and temperatures, confirming ohmic contact and negligible sample heating caused by the measurement current. The resistivity was determined from the measured sheet resistance using a geometric correction factor [66] and the thickness measured by SEM.

First-principles calculations were performed using the Vienna *ab initio* simulation package (VASP), employing periodic boundary conditions, a plane wave basis set, the Perdew-Burke-Ernzerhof (PBE) generalized gradient approximation (GGA) exchange correlation functional [67], and the projector-augmented wave method

[68]. A 550 eV cut-off energy for the plane-wave basis set and a 4 \times 4 \times 4 Γ -centered k -point grid for cubic and hexagonal supercells with 32 and 36 cations yield energy convergence of < 1 meV/atom. Ti 3s, 3p, 3d, and 4s electrons are explicitly calculated using the Ti_{sv} pseudo potential provided with the VASP package. The formation energy E_f and lattice constants of cubic and hexagonal TiC_x with $0 \leq x \leq 1$ were determined by removing C atoms from rock-salt structure TiC and adding interstitial C to hexagonal close-packed Ti, respectively, while $x > 1$ was simulated by adding C interstitials and C clusters to rock-salt TiC. More specifically, (i) cubic supercells with 32 Ti atoms on fcc sites and $N_C = 0, 8, 16, 24$, or 32 C atoms on anion sites were computed by simultaneously relaxing atomic positions and the lattice constant a , while retaining the supercell shape to represent the overall cubic structure for direct comparison with experiment. Three independent simulations were done for a given $N_C (= 8, 16$ or $24)$ with different random anion site occupations. This approach was chosen instead of the Special Quasirandom Structures approach [69], because the variation in E_f and a from the three simulations provides an indication of the uncertainty in the determined energy and lattice constant associated with the random distribution of C atoms on anion sites. In addition, ordered arrays with $N_C = 0, 16$, and 32 yielding fcc Ti, cubic Ti₂C, and rock-salt TiC were computed. (ii) Similarly, hexagonal supercells with 36 Ti atoms on hcp sites and 0, 9, 18, 27, or 36 C atoms on octahedral interstitial sites were computed by iteratively relaxing atomic positions and lattice constants a and c . That is, the a -to- c ratio was allowed to relax but the supercell was forced to remain hexagonal. Three random C occupancies were simulated for a given N_C . Multiple ordered arrangements with $N_C = 16$ were explored, with the lowest energy configuration having an ordered 75 and 25% occupation on alternate close-packed anion-site planes. In addition, isolated C interstitials and interstitial pairs in hcp Ti were simulated using $N_{Ti} = 36$ and $N_C = 1$ and 2, and varying the C-C distance for the latter case. (iii) Overstoichiometric TiC_x ($x > 1$) was explored using as starting point a 64-atom rock-salt structure TiC supercell with $N_{Ti} = N_C = 32$. A total of 78 atomic arrangements were independently relaxed in search for the lowest energy configurations, starting with single C interstitials in tetrahedral interstitial or split-interstitial sites ($N_{Ti} = 32, N_C = 33$), followed by configurations with few involved atoms such as anti-site substitutions ($N_{Ti} = 31, N_C = 33$) or carbon-pairs or triplets on a Ti site ($N_{Ti} = 31, N_C = 34/35$), and small C-clusters or graphitic rings involving 4–10 C atoms (e.g. $N_{Ti} = 28, N_C = 40$). In addition, the energy of extended 2D defects such as a graphene plane in contact with a TiC(001) surface was also calculated using various appropriate supercells.

The calculated zero temperature energy of the most relevant configurations is presented in this paper in units of eV/atom using hcp Ti and rock-salt TiC as reference states. This allows to clearly plot the energy vs composition for $0 \leq x \leq 1$ for different phases which would be hard to present because they would converge to nearly a single line if using the more conventional approach with elemental phases (hcp Ti and graphite) as standard states. More specifically, the calculated formation energy of rock-salt TiC is -0.824 eV per atom if hcp Ti and graphite are used as standard states. Conversely, here we set the energy for hcp Ti and for TiC to zero, while the energy for graphite is $+0.824$ eV/atom. For this purpose, the formation energy per atom for a configuration with e.g. $N_{Ti} = 32$ and $N_C = 8$ is obtained by subtracting $N_{Ti} - N_C = 24$ times the calculated energy/atom of hcp Ti and $N_C = 8$ times the calculated energy per formula unit of TiC from the calculated total energy of the configuration. We note that this method also provides more accurate formation energies because it does not require a calculation of the energy of graphite, which has an expected 20–60 meV/atom error from using conventional PBE GGA without correcting for Van der Waals interactions [70].

In addition, in order to provide a first estimate of the temperature effect on the relative Gibbs free energy, we calculate the configurational entropy associated with the random arrangement of C atoms on anion sites using $S = -k_B[x \ln x + (1-x) \ln(1-x)]$ where k_B is Boltzmann's constant, x is the fraction of occupied anion sites which is equal to the C-to-Ti ratio x , and S is the entropy per anion site. Using the experimental growth temperature $T_s = 1100 \text{ }^\circ\text{C} = 1373 \text{ K}$, we calculate a Gibbs free energy correction $-TS = -53 \text{ meV}$ per atom for the example configuration above with $N_{Ti} = 32$ and $N_C = 8$. We reiterate that this entropy correction is a first-level approximation to the effect of temperature, while other contributions including vibrational entropy and thermal expansion are neglected because of the considerable computational cost associated with true finite-temperature methods.

3. Results and discussion

Fig. 1(a) is a plot of the measured C-to-Ti ratio x in the deposited TiC_x layers as a function of $f_{\text{CH}_4} = 0.4\text{--}8\%$. It includes the results from both XPS and EDS analyses, plotted as magenta circles and blue squares, respectively. The two independent measurement methods are in good agreement. We attribute the small difference between the values from the two methods to preferential sputtering during surface cleaning for XPS measurements [71] and/or the experimental uncertainties for light element determination using EDS as stated in Section 2. Thus, for the remainder of the paper, we use the average values from these two methods. The plotted C-to-Ti ratio increases nearly linearly from $x = 0.08$ to 0.24, 0.5, 1.0, 1.5 to 1.8 with increasing $f_{\text{CH}_4} = 0.4, 1, 2, 4, 6$ and 8% . We attribute the increasing C-content to chemisorbed CH_x fragments, graphitic C, and/or carbide on the Ti target surface which forms through impinging CH_4^+ ions. The carbon is then sputtered from this target surface as C-atoms, C-clusters, or carbide molecules together with Ti atoms to form the TiC_x layer. The CH_4^+ ion flux towards the target, and therefore also the C-flux towards the substrate, are expected to be proportional to f_{CH_4} , resulting in the observed linear increase in Fig. 1(a). The increasing C on the target surface also results in a reduction in the deposition rate from 11 to 7 nm/min with increasing $f_{\text{CH}_4} = 0.4\text{--}4\%$. This is attributed to a reduction in the secondary electron yield and a lower sputtering rate for the C-contaminated Ti target surface. We note that the layer growth rate increases again from 7 to 9 nm/min with increasing $f_{\text{CH}_4} = 4\text{--}8\%$, which may be due to an increasing CH_4 sticking probability for layers containing carbon clusters on the growing film surface, resulting in the inclusion of lower-density amorphous carbon for $f_{\text{CH}_4} = 6$ and 8% which yields $\text{TiC}_{1.5}$ and $\text{TiC}_{1.8}$, respectively.

Fig. 1(b) is a representative XPS spectrum from a carbon-rich sample, showing the C 1s peak for a $\text{TiC}_{1.8}$ film after Ar^+ sputter-cleaning. The purple solid line represents the measured intensity while the orange, red, and cyan lines are obtained from curve fitting, indicating C-Ti, C-Ti*, and C-C peaks, respectively. The C-Ti peak is from carbon in bulk TiC. The C-Ti* peak is attributed to C near the TiC surface where the smaller number of Ti neighbors reduces the charge transfer and therefore increases the binding energy [72]. The C-C peak from carbon in graphitic and/or amorphous C is considerably broader than the C-Ti and the C-Ti* peaks, which is attributed to splitting into sp^2 (284.4 eV) and sp^3 (285.2 eV) hybridized peaks [73] as marked with dashed vertical lines and indicated by the two cyan fitting curves. The area ratio of sp^3 vs sp^2 C-C peaks provides an estimate of 24% for the fraction of sp^3 bonding within the secondary carbon phase in the $\text{TiC}_{1.8}$ film, in good agreement with 28% from the Raman analysis presented below. In addition, the C-C peak corresponds to 50% of the total C 1s intensity, indicating an atomic fraction of carbon in the amorphous C phase $f_{a-C} = 50\%$, in reasonable agreement with $44 \pm 3\%$ expected for $x = 1.8$. We estimate a volume frac-

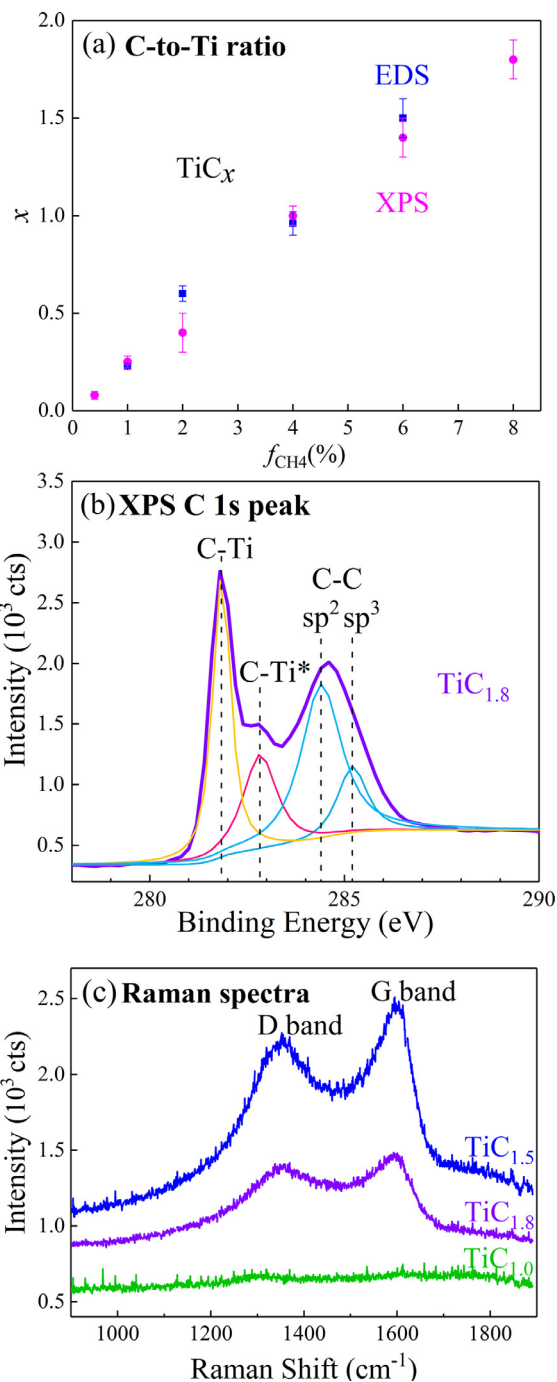


Fig. 1. (a) The C-to-Ti ratio x in TiC_x layers deposited using an Ar-CH_4 mixture with a varying methane fraction $f_{\text{CH}_4} = 0.4\text{--}8\%$. Results from XPS and EDS measurements are denoted as magenta circles and blue squares, respectively. (b) XPS C 1s peak from a $\text{TiC}_{1.8}$ film. (c) Raman spectra from $\text{TiC}_{1.0}$, $\text{TiC}_{1.5}$ and $\text{TiC}_{1.8}$ films.

tion $V_{a-C} = 0.24 \pm 0.05$ of the secondary a-C:H phase in the $\text{TiC}_{1.8}$ layer from $f_{a-C} = 44\%$ by assuming an amorphous carbon density $\rho^* = 1.92\text{--}3.29 \text{ g/cm}^3$ [74] corresponding to an atomic density of 9.63 to $16.5 \times 10^{22} \text{ cm}^{-3}$, while the C atomic density in rock-salt TiC is $4.944 \times 10^{22} \text{ cm}^{-3}$. Corresponding XPS measurements were done for all layers in this study. The C 1s peaks from the $\text{TiC}_{1.5}$ layer indicates a secondary carbon phase with 31% sp^3 bonding and a $f_{a-C} = 40\%$, in reasonable agreement with $f_{a-C} = 33 \pm 4\%$ from the overall composition which also yields $V_{a-C} = 0.16 \pm 0.04$ for $\text{TiC}_{1.5}$. In contrast, no XPS peak associated with C-C bonds could be detected for samples with $x \leq 1.0$ (with the exception of

a small peak due to redeposited surface carbon after Ar⁺ sputter-cleaning of the TiC_{1.0} sample), indicating that all carbon for layers with a C-to-Ti ratio below 1.0 is contained within the cubic carbide phase, as expected.

Fig. 1(c) are Raman spectra for TiC_{1.0}, TiC_{1.5} and TiC_{1.8} films in the range of 900–1900 cm⁻¹. The carbon-rich TiC_{1.5} and TiC_{1.8} films exhibit clear D and G band features at 1350 and 1590 cm⁻¹ which are attributed to the A_{1g} D breathing mode and the E_{2g} G mode from amorphous carbon [75]. Double-Gaussian curve fitting yields an intensity ratio I(D)/I(G) = 1.7 and 2.5 for TiC_{1.5} and TiC_{1.8}, respectively, indicating an sp³ fraction of 32 and 28% based on the reported I(D)/I(G) vs sp³ relationship [75]. These fractions of sp³ hybridized bonding are in good agreement with the 31% and 24% determined by XPS. In contrast, the stoichiometric TiC_{1.0} film shows no obvious peak in the detected Raman shift range, confirming that the amorphous carbon content in the stoichiometric x = 1.0 layer is negligible. We note that the a-C phase for x ≥ 1.5 layers may contain hydrogen which is not easily quantified and stems from the CH₄ processing gas. We also note that this source of possible hydrogen impurities can be removed by replacing the reactive deposition process with co-sputtering from Ti and graphite targets in pure Ar. However, our test experiments with this latter approach resulted in undesired formation of C clusters in lieu of carbide such that this approach was not further explored in this study.

Fig. 2 shows typical x-ray diffraction results from TiC_x layers deposited on MgO(001) with f_{CH4} = 0.4 to 8%, yielding C-to-Ti ratios x = 0.08–1.8. The θ–2θ patterns in Fig. 2(a) are obtained using a divergent beam Bragg-Brentano geometry. They are plotted over a limited 2θ = 39–44.5° range to highlight the primary substrate and layer peaks, and are offset vertically for clarity purposes. In addition, the plotted intensity near the strong substrate reflections is reduced by an order of magnitude (× 0.1) for 2θ = 42.7–43.3° to display both the substrate and layer peaks within the same plot. The TiC_{0.08} layer deposited with f_{CH4} = 0.4% (red curve) shows a doublet peak at 2θ = 42.909° and 43.020° due to the MgO 002 reflection of the CuK_{α1} and CuK_{α2} lines with wavelengths λ = 1.5406 and 1.5444 Å, respectively, and a corresponding doublet around 42° from the TiC 002 reflection, with the CuK_{α1} peak at 2θ = 41.957°. In addition, there is a 15-times weaker peak at 2θ = 39.811° which is made visible in Fig. 2(a) by multiplying the plotted intensity around 2θ = 40° fifty times. This peak is attributed to the 10 $\bar{1}$ 1 reflection of hexagonal Ti which has an expected 2θ = 40.227° (JCPDS 001–1197). Our measured angle is 1% smaller, indicating an expanded lattice constant along the growth direction which is attributed to interstitial C in hexagonal Ti as discussed below. No other peaks from hcp Ti could be detected over the entire measured 2θ = 5–85° range, suggesting a preferred orientation which is confirmed by the local epitaxy detected by the RSM presented below. The pattern for the TiC_{0.24} layer deposited with f_{CH4} = 1% (orange line in Fig. 2) exhibits a substrate feature as for x = 0.08, a TiC 002 peak at 2θ = 41.930° and a weak Ti 10 $\bar{1}$ 1 reflection at 2θ = 39.81°. The intensity of the Ti 10 $\bar{1}$ 1 peak is smaller than for TiC_{0.08}, suggesting a decreasing volume fraction of the hcp Ti impurity phase. The TiC peak is shifted towards the left, indicating an increasing out-of-plane lattice constant a_⊥ with increasing carbon incorporation. Increasing the carbon content further to x = 0.5, 1.0, 1.5 and 1.8 leads to XRD patterns which continue to be dominated by TiC 002 and MgO 002 peaks. No intensity from an hcp Ti impurity phase can be detected over the entire measured 2θ = 5–85° for x ≥ 0.5. However, the TiC_{1.0} sample shows a minor intensity of 111-oriented (misoriented) TiC grains. The measured TiC 002 peak intensity increases from x = 0.08 to 1.0, but then decreases again for x = 1.5 and 1.8, suggesting a maximum in the crystalline quality for the stoichiometric TiC_{1.0} layer. The peak position continuously moves towards smaller 2θ values, indi-

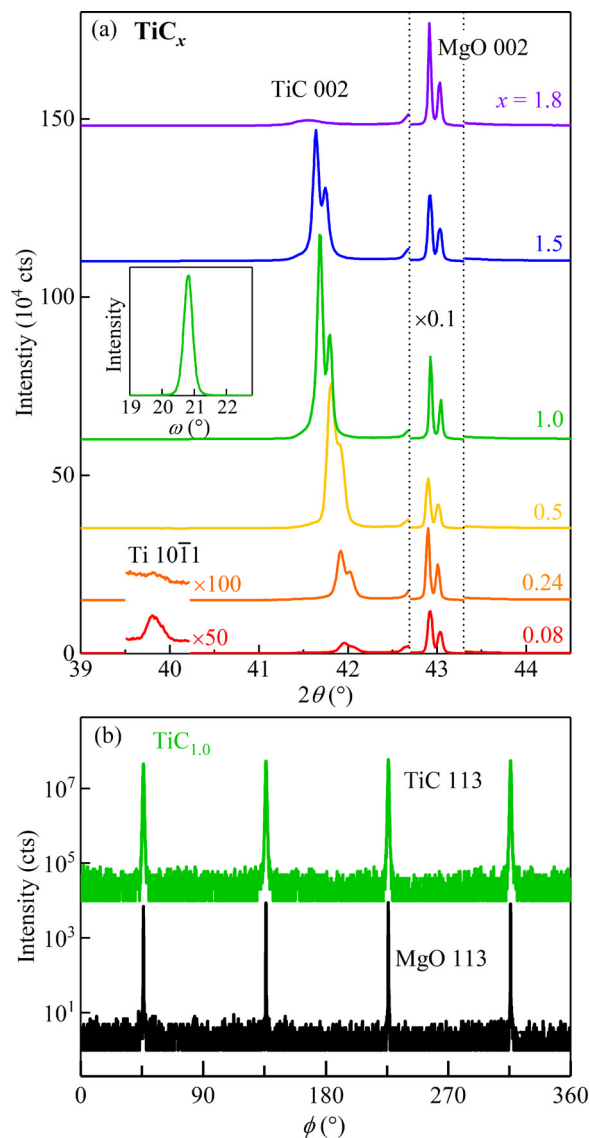


Fig. 2. X-ray diffraction (a) θ – 2θ patterns from TiC_x/MgO(001) layers with x = 0.08–1.8, with the patterns from different samples offset by a constant intensity and scaled over selected sections as labeled, and (b) ϕ -scans for TiC 113 and MgO 113 reflections from a TiC_{1.0} layer with the TiC signal offset by a factor of 10⁴. The inset in (a) shows a representative ω rocking curve from the TiC 002 reflection of the TiC_{1.0} layer.

ating a continued trend towards larger lattice constants with increasing C content, as discussed below. The inset in Fig. 2(a) shows an ω -rocking curve of the TiC 002 reflection from the TiC_{1.0} layer, obtained using a parallel beam monochromatic x-ray source. The peak has a full-width at half-maximum $\Gamma_{\omega} = 0.33^{\circ}$, indicating a good out-of-plane crystalline alignment. Measurements done on all samples (not shown) indicate relatively narrow rocking curves with $\Gamma_{\omega} < 1^{\circ}$ for x = 0.08–1.5, suggesting that these layers are epitaxial TiC_x(001). In contrast, $\Gamma_{\omega} = 3.7^{\circ}$ for TiC_{1.8}, indicating a considerable decrease in crystalline quality at large C-content, consistent with the weak TiC 002 peak in Fig. 2(a) for x = 1.8. The epitaxial growth is confirmed by XRD ϕ -scans. Fig. 2(b) displays typical ϕ -scans from the TiC_{1.0} layer, obtained using an X-ray point source with a substrate tilt $\chi = 54.7^{\circ}$ and $2\theta = 35.9$ and 36.947° to detect the TiC 113 (green) and MgO 113 (black) reflections, respectively. The measured intensity is plotted in a logarithmic scale vs the azimuthal angle $\phi = 0$ – 360° and is offset by a factor of 10⁴ for the layer pattern for clarity purposes. Both substrate and layer exhibit

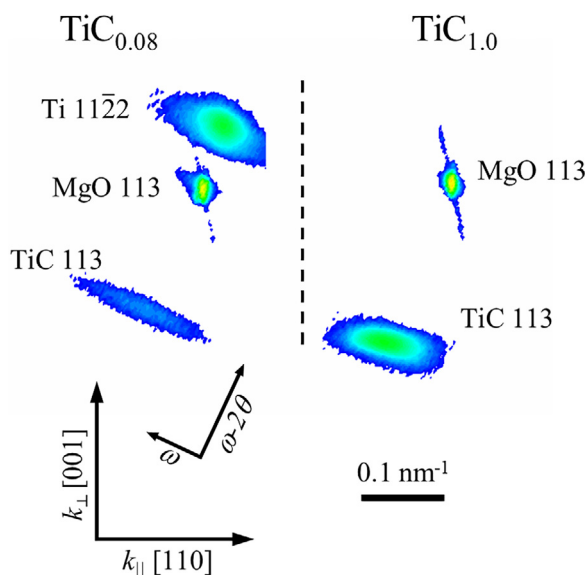


Fig. 3. XRD reciprocal space maps showing MgO 113, TiC_x 113, and Ti 11 $\bar{2}2$ reflections from two TiC_x(001)/MgO(001) layers with $x = 0.08$ and 1.0.

a four-fold symmetry with aligned peaks at 45, 135, 225, and 315°, indicating a cube-on-cube epitaxial relationship with (001)_{TiC} || (001)_{MgO} and [100]_{TiC} || [100]_{MgO}. Similar ϕ -scans were performed for all samples and indicate epitaxial TiC_x growth except for the TiC_{1.8} film. This is consistent with the measured Γ_ω and suggests a breakdown of epitaxy for large $x \geq 1.8$ which we attribute to nucleation of carbide grains with random in-plane orientation on top of segregated carbon clusters for $f_{\text{CH}_4} = 8\%$.

Fig. 3 shows two representative XRD RSMs from TiC_x/MgO(001) layers with $x = 0.08$ and 1.0, showing the MgO 113, TiC_x 113 and Ti 11 $\bar{2}2$ reflections. The measured intensity is indicated by blue-to-green-to-yellow isointensity contours in a logarithm scale, and plotted in reciprocal space where the vertical and horizontal vectors $k_\perp = 2\sin\theta \cos(\omega-\theta)/\lambda$ and $k_\parallel = 2\sin\theta \sin(\omega-\theta)/\lambda$ point along the out-of-plane MgO[001] and the in-plane MgO[110] directions, respectively. The plot also contains a scale bar for the reciprocal length and arrows to indicate the experimental $\omega-2\theta$ and ω scanning directions, which are rotated by 25.24° with respect to k_\perp and k_\parallel . The strongest peaks (yellow) in both maps are from the substrate 113 reflection. The weak streaks from top-left to bottom-right across the MgO 113 peaks are due to electronic noise from a fully open line detector. The asymmetric elongation along the ω direction in the left map is attributed to the mosaic spread in the substrate. The TiC_{0.08} layer shows a strong Ti 11 $\bar{2}2$ reflection, indicating that the hexagonal Ti phase exhibits local epitaxy on MgO(001) despite a large Ti 10 $\bar{1}1$ rocking curve width ($\Gamma_\omega > 4^\circ$). The peak position yields lattice constants $a = 0.2983$ nm and $c = 0.4685$ nm. These values are larger than the reported $a = 0.2951$ nm and $c = 0.4670$ nm for hcp Ti, indicating a 2.5% larger unit cell volume which indicates carbon incorporation into the Ti lattice corresponding to a hexagonal TiC_x with $x = 0.065$, based on our first-principles calculations presented below. This peak has an elliptical shape with elongations along the ω direction due to mosaicity and along the $\omega-2\theta$ direction due to crystalline defects and/or strain fluctuations. The weaker peak in the left panel is from the TiC 113 reflection and is shifted along the negative $\omega-2\theta$ direction with respect to the substrate peak, indicating a fully relaxed layer. Its position at $k_\perp = 6.974$ nm⁻¹ and $k_\parallel = 3.289$ nm⁻¹ provides values for the lattice constants perpendicular and parallel to the substrate surface $a_\perp = 3 / k_\perp$ and $a_\parallel = \sqrt{2} / k_\parallel$, respectively, as discussed below. The peak width Δk_\parallel

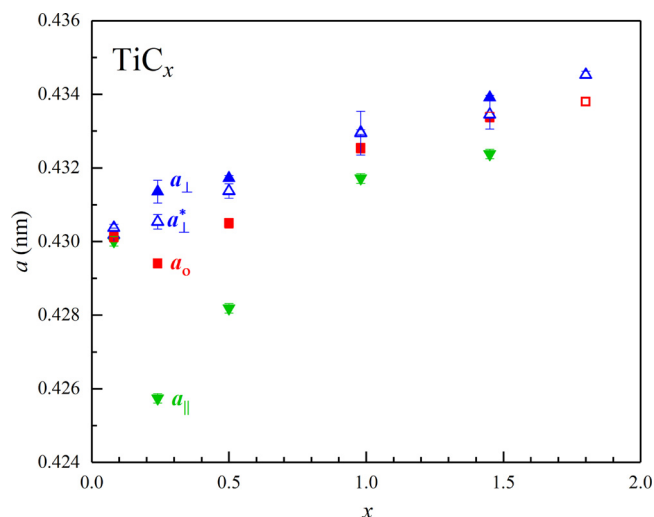


Fig. 4. Out-of-plane and in-plane lattice constants a_\perp and a_\parallel determined from reciprocal space maps, out-of-plane lattice constants a_\perp^* determined from symmetric $\theta-2\theta$ scans, and relaxed lattice constants a_0 vs the C-to-Ti ratio x in TiC_x layers.

in the in-plane direction is 0.039 nm⁻¹, yielding an in-plane coherence length $\xi_\parallel = 1 / \Delta k_\parallel = 26$ nm which is two times larger than the 13 nm coherence length determined from the 0.94° ω rocking curve width of the symmetric TiC 002 peak. This deviation is likely due to different x-ray beam positions for the two measurements such that the broadening caused by the substrate mosaicity and possible associated secondary domain peaks varies. The map for the TiC_{1.0} layer shows only the TiC 113 peak. Its position at $k_\perp = 6.923$ nm⁻¹ and $k_\parallel = 3.276$ nm⁻¹ indicates a slight (nearly negligible) compressive strain of $\varepsilon_\parallel = -0.2\%$. The peak width yields an in-plane coherence length $\xi_\parallel = 1 / 0.032$ nm⁻¹ = 31 nm, in good agreement with the 38 nm determined from the rocking curve shown in Fig. 2. Similar reciprocal space maps are obtained for all samples with $x = 0.08-1.8$, confirming the epitaxial growth of TiC_x for $x = 0.08-1.5$. However, no 113 layer peak could be detected for TiC_{1.8}, consistent with the $\theta-2\theta$ and ϕ -scan data which indicate a 001-preferred orientation with random in-plane orientation for $x = 1.8$.

Fig. 4 is a plot of the lattice constant a as a function of the total C-to-Ti ratio x in the TiC_x films. The out-of-plane lattice constant a_\perp and in-plane lattice constant a_\parallel determined from the RSMs are marked as solid blue and green triangle symbols, respectively. The plot also includes the out-of-plane lattice constant a_\perp^* determined from symmetric $\theta-2\theta$ scans obtained using a monochromatic parallel beam diffraction geometry shown as open blue triangles, and the relaxed lattice constant a_0 as red solid squares. The latter is determined using $a_0 = (a_\perp - \nu a_\perp + 2\nu a_\parallel)/(1 + \nu)$ where a_\perp and a_\parallel are the values measured from the RSMs and ν is the Poisson's ratio which is assumed to be independent of x and equal to 0.21, the value reported for stoichiometric TiC [64]. We note that the plot does not show RSM data from the TiC_{1.8} film, because no peak could be detected in the ϕ -scan and RSM map due to the low crystalline quality and likely a random in-plane orientation for this layer. The measured a_\perp increases monotonically from 0.4302 to 0.4339 nm as x increases from 0.08 to 1.5, consistent with the continuous shift to lower 2θ angles of the TiC 002 reflections in Fig. 2(a). These a_\perp values are in excellent agreement with a_\perp^* measured from the symmetric scans, with deviations of only 0.007–0.2% between the two datasets. The measured a_\parallel drops initially from 0.4300 nm for TiC_{0.08} to 0.4257 nm for TiC_{0.24}, followed by a monotonous increase to 0.4324 nm for TiC_{1.5}. Similarly, the relaxed lattice constant initially decreases from 0.4301 nm for TiC_{0.08}

to 0.4294 nm for $\text{TiC}_{0.24}$, followed by an increase to $a_0 = 0.4305$, 0.4325, 0.4334, and 0.4339 nm for $\text{TiC}_{0.5}$, $\text{TiC}_{1.0}$, $\text{TiC}_{1.5}$ and $\text{TiC}_{1.8}$, respectively. These values will be discussed in detail below, after presenting the first-principles calculation results. The last value ($x = 1.8$) is indicated in Fig. 4 by an open red square because it could not be directly obtained from the reciprocal space map (due to insufficient intensity) but instead, is determined from the measured $a_{\perp}^* = 0.4345$ nm and assuming the same slight compressive strain as for the $x = 1.5$ sample.

The overlapping datapoints for $x = 0.08$ in Fig. 4 indicate that the carbide within the layer with $x = 0.08$ is fully relaxed. In contrast, the measured strain is largest ($\varepsilon_{\perp} = 0.5\%$) for $x = 0.24$ and then continuously decreases to $\varepsilon_{\perp} = 0.3\%$, 0.1% , and 0.1% for $x = 0.5$, 1.0 , and 1.5 , respectively. This expansion along the growth direction is due to an in-plane compressive stress which is primarily attributed to a mismatch in the thermal expansion coefficients between the substrate and the layers. The reported linear thermal expansion coefficient is $1.4 \times 10^{-5} \text{ K}^{-1}$ for MgO [76] and $8.4 \times 10^{-6} \text{ K}^{-1}$ for nearly stoichiometric $\text{TiC}_{0.95}$ [77]. This results in an expected -0.6% compressive thermal strain during cooling after deposition from $1100 \text{ }^{\circ}\text{C}$ to room temperature. The measured compressive strain $\varepsilon_{\parallel} = -0.2\%$ for the stoichiometric $\text{TiC}_{1.0}$ film is three times smaller, suggesting considerable relaxation during cooling. In contrast, the $\text{TiC}_{0.24}$ layer has a large compressive strain of $\varepsilon_{\parallel} = -0.9\%$, suggesting negligible relaxation which may be due to dislocation pinning by the large density of C-vacancies in the carbide as well as small secondary hcp phase inclusions in this layer. Conversely, the $\text{TiC}_{0.08}$ layer is fully relaxed, indicating that the larger fraction of metallic (more ductile) hcp grains within this layer facilitates relaxation during cooling. We note that these strain arguments are semi-quantitative, as the thermal expansion coefficient is composition dependent and is likely increasing with decreasing x , based on the reported $\sim 11 \times 10^{-6} \text{ K}^{-1}$ for metallic Ti between 25 and $700 \text{ }^{\circ}\text{C}$ [78]. We also note that the lattice misfit between TiC_x films and MgO substrates increases from 1.9% for $\text{TiC}_{0.24}$ to 2.9% for $\text{TiC}_{1.5}$ layers. This misfit is sufficiently large that we expect the layers to be nearly fully relaxed during growth.

Fig. 5 is a plot of the calculated formation energy E_f per atom vs composition of cubic (red squares) and hexagonal (navy hexagons) TiC_x , where the reference (zero energy) states are hcp Ti and rock-salt structure TiC as described in Section 2. The bottom axis indicates the compositional parameter y , as defined by $\text{Ti}_{1-y}\text{C}_y$. This new notation is introduced here such that connecting the lowest energy configurations directly provides the convex hull, as indicated by the black dashed line. In contrast, the compositional parameter x which is used throughout this paper and is defined by TiC_x is shown as top x -axis. The zero-temperature convex hull connects hcp Ti at $x = 0$ with an ordered cubic Ti_2C with $E_f = -0.108 \text{ eV}$ at $x = 0.5$, rock-salt structure TiC_x with C atoms on random anion sites for $0.5 < x < 1$ including the calculated $E_f = -0.079 \text{ eV}$ at $x = 0.75$, stoichiometric rock-salt TiC with $E_f = 0$ (by definition, see Section 2) at $x = 1.0$, and graphite with $E_f = 0.823 \text{ eV}$ at $x = \infty$ ($y = 1$) outside the plotted range. Thus, the zero-temperature convex hull predicts phase separation into hexagonal and cubic phases for $x = 0-0.5$, cubic TiC_x for $0.5 \leq x \leq 1.0$, and phase-separated cubic TiC and graphitic C for $x > 1$. This is in perfect agreement with the experimentally detected phases shown in Figs. 2(a) and 1(b,c), namely both hexagonal and cubic phases for $x = 0.08$ and 0.24 , phase-pure cubic TiC_x for $x = 0.5$ and 1.0 , and an increasing C-C bond density and decreasing crystalline quality of the cubic phase with increasing $x = 1.5$ and 1.8 , indicating graphitic and/or amorphous carbon at high x . The plotted $E_f = -0.079 \text{ eV}$ for the disordered $\text{TiC}_{0.75}$ is the average energy from three independent calculations. Their standard deviation is only 0.005 eV , which approximately matches the plotted symbol size, such that no error bars are shown in

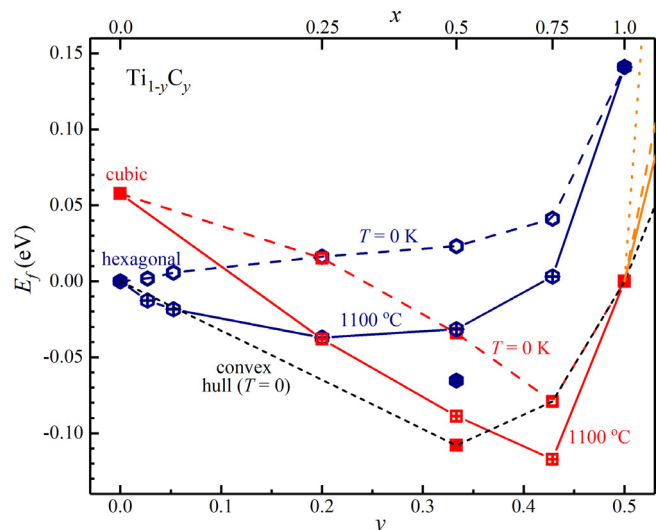


Fig. 5. The calculated formation energy per atom E_f for $\text{Ti}_{1-y}\text{C}_y$ in the rocksalt (red) and hexagonal close-packed (navy) structures at 0 K and $1100 \text{ }^{\circ}\text{C}$. Solid symbols denote ordered structures. The reference states are hcp Ti and stoichiometric rocksalt-structure TiC. The zero-temperature convex hull is indicated by a black dashed line while the orange solid, dashed and dotted lines denote energies for TiC containing graphene sheets, C-pairs on cation sites, and interstitial C, respectively. The top x -axis indicates the alternative compositional parameter x for TiC_x as used throughout the paper.

Fig. 5. The open square and open hexagonal symbols connected by dashed lines represent the calculated zero-temperature formation energies for the cubic and hexagonal phases, while the symbols with center-crosses that are connected with solid lines are the energies which are corrected by a $-TS$ term for the configurational entropy, as described in Section 2. This entropy term considerably reduces the energy towards or below the zero- T convex hull and is therefore expected to affect the phase formation and composition. For example, the energy for cubic $\text{TiC}_{0.75}$ with random C vacancies on anion sites at 0 K is 0.025 eV/atom lower than the average energy of ordered Ti_2C and TiC phases, and is further reduced by 0.038 eV/atom with the $-TS$ correction, indicating a strong preference for a disordered TiC_x cubic phase in comparison to a mixture of ordered Ti_2C and TiC. Even at $x = 0.5$, the $-TS$ -corrected energy for the disordered $\text{TiC}_{0.25}$ is only 0.016 eV/atom above the ordered Ti_2C phase. Thus, considering also kinetic barriers for ordering, we expect phase-pure disordered cubic TiC_x for the entire $0.5 < x \leq 1.0$ range. Similarly, the $-TS$ correction reduces the energy for $\text{TiC}_{0.25}$ with random anion site occupation in cubic and hexagonal structures from 0.080 to 0.081 eV above the convex hull at zero temperature to only 0.027 and 0.028 eV above the convex hull at $T_s = 1100 \text{ }^{\circ}\text{C}$. Such small energies above the convex hull suggest a considerable probability for formation of non-equilibrium phases, in particular a cubic phase with $x < 0.5$, as indicated by the measured cubic lattice constant and discussed below. At low C content, the corrected energies for hexagonal $\text{TiC}_{0.028}$ and $\text{TiC}_{0.056}$ are slightly below the zero-temperature convex hull. As a result, the solid navy line in Fig. 5 for the temperature-corrected hexagonal TiC_x crosses the dashed black line from the $T = 0$ convex hull at a finite $x = 0.063$, indicating a predicted C-solubility in hcp Ti at $T_s = 1100 \text{ }^{\circ}\text{C}$. This solubility limit is in excellent agreement with the estimated C content in the hexagonal TiC_x phase in layers deposited with a low f_{CH4} . More specifically, the measured unit cell volume of the hexagonal phase within the $\text{TiC}_{0.08}$ layer is 2.5% larger than for pure hcp Ti, while the corresponding first-principles calculated volume increases for hexagonal $\text{TiC}_{0.028}$ and $\text{TiC}_{0.056}$ are 1.1% and 2.1% , yielding an extrapolated $x = 0.065$ for the experimental 2.5% volume increase. The calculated $x = 0.063$ solubility

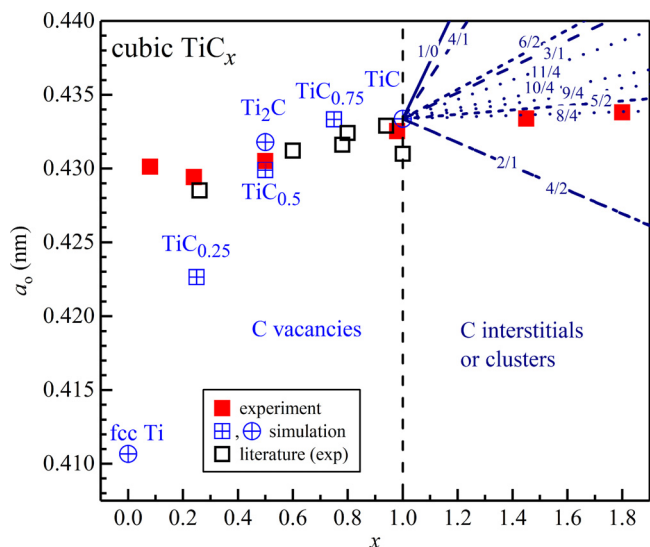


Fig. 6. Calculated lattice constants a_0 vs x for cubic TiC_x with random (square cross symbol) and ordered (circle cross symbol) occupation on anion sites, predicted a_0 vs $x \geq 1$ (navy lines) for over-stoichiometric TiC_x containing defect structures with X_c carbon interstitials and V_{Ti} Ti vacancies labeled X_c/V_{Ti} , experimentally measured relaxed a_0 from this work (red squares), and experimental literature values (open black squares) from Refs. [10,51,54,79].

limit is four times larger than the previously reported C solubility $x = 0.016$ in hexagonal α -Ti which [47], however, is limited to temperatures below the 920 °C phase transition temperature from hexagonal α -Ti to bcc β -Ti. Correspondingly, we attribute the high $x = 0.065$ to an elevated C solubility in meta-stable hexagonal Ti at 1100 °C and kinetic suppression for C out-diffusion during cooling. We note here that our predicted solubility has a relatively large uncertainty since even a small temperature change from e.g. 1100 °C to 920 °C leads to a substantial solubility reduction from 0.063 to 0.042.

The orange lines in Fig. 5 for $x > 1.0$ indicate the calculated energy vs composition for rock-salt TiC containing single graphene sheets (solid line), C-pairs on cation sites (dashed line), and C interstitials on tetragonal sites (dotted line). These lines are well above the convex hull which is plotted as black dashed line and is defined by stoichiometric TiC and graphite. This indicates that these configurations are thermodynamically unstable against phase separation into TiC and graphite. In fact, all 78 explored carbon-cluster configurations have energies which are well above the convex hull. More specifically, the calculated formation energy for a C interstitial in TiC is 3.891 eV with TiC and graphite as reference states. One of the most stable configurations is a C-pair that replaces a Ti on a cation site. It has a formation energy of 5.490 eV and effectively accounts for three excess C atoms, yielding 1.830 eV per C atom. Larger C clusters do not substantially reduce this energy, with for example 1.693 and 1.639 eV per excess C for configurations with 4 C atoms on 2 neighboring cation sites or 9 added C atoms on 4 Ti sites. The plotted energy for a graphene monolayer has a lower energy than C clusters but has a large expected kinetic barrier for formation and also represents the nucleation site for phase separated graphite which may form on top of C that segregates to the surface of TiC during layer growth to form a graphene surface layer. That is, all C interstitials and clusters within TiC are energetically unfavorable and only form due to kinetic barriers for the phase separation into graphite or amorphous C. However, if C is within the TiC matrix, it affects the measured TiC_x lattice constant, as discussed in the following.

Fig. 6 is a plot of relaxed lattice constants a_0 as a function of the C-to-Ti ratio x in cubic TiC_x from both experiments and first-

principles calculations. The red squares are the measured a_0 values reproduced from Fig. 4, the open black squares denote measured values from the literature [10,51,54,79], and the blue symbols and navy lines represent the lattice constants from our first-principles simulations for $x \leq 1.0$ and $x > 1.0$, respectively. More specifically, the circular data points indicate the calculated lattice constants for ordered rock-salt-type structures with $x = 0, 0.5$, and 1, namely face-centered cubic (fcc) Ti with $a_0 = 0.4107$ nm, cubic ordered Ti_2C with $a_0 = 0.4318$ nm, and stoichiometric rock-salt-structure TiC with $a_0 = 0.4334$ nm. The blue open squares with center crosses indicate the predicted lattice constants for $\text{TiC}_{0.25}$, $\text{TiC}_{0.5}$, and $\text{TiC}_{0.75}$ with random C occupation on anion sites, indicating an almost linear increase with $a_0 = 0.4226$, 0.4299 and 0.4333 nm, respectively. The navy lines for $x > 1$ are the predicted a_0 for various carbon interstitial and carbon cluster configurations, where the labels on top of the lines X_c/V_{Ti} indicate the number of C interstitials X_c and Ti vacancies V_{Ti} that define the defect structure within stoichiometric rock-salt-structure TiC. For example, the solid line labeled “1/0” indicates the lattice constant of TiC_x where the deviation above the stoichiometric $x = 1$ is accounted for by individual C interstitials (i.e. $X_c = 1$) while all cation sites are occupied by Ti, thus $V_{\text{Ti}} = 0$. This line has a steep positive slope $da_0/dx = 0.039$ nm, indicating that C interstitials in TiC cause a considerable lattice expansion. The dashed lines labeled “2/1”, “3/1” and “4/1” are for small carbon clusters where two, three, or four carbon atoms ($X_c = 2, 3$ or 4) replace one Ti on a cation site ($V_{\text{Ti}} = 1$). The missing Ti atom causes a reduction in the lattice constant, leading to a negative $da_0/dx = -0.008$ nm for $X_c = 2$, while three or four C atoms on a single cation site more than compensate the volume reduction from the missing Ti, yielding positive $da_0/dx = 0.009$ and 0.028 nm, respectively. The plotted short-dash and dotted lines are for $V_{\text{Ti}} = 2$ and 3, respectively, with a correspondingly larger number of excess carbon atoms $X_c = 4-11$. We note that isolated Ti vacancies are not considered here because their calculated formation energy of 6.845 eV is nearly twice that of isolated C interstitials. This is quite different from isostructural transition metal nitrides where cation vacancies are the lowest-energy overstoichiometric ($x > 1$) defects [80-83].

We now discuss the results presented in Fig. 6. That is, we quantitatively compare measured and predicted lattice constants to gain insight into phase formation in TiC_x . For this purpose, we note that the measured lattice constants (red solid squares) are for the epitaxial rocksalt TiC_x phase, but that only the $\text{TiC}_{0.5}$ and $\text{TiC}_{1.0}$ layers are phase-pure rocksalt structure carbides, while the $\text{TiC}_{0.08}$ and $\text{TiC}_{0.24}$ layers additionally contain an hcp Ti phase and that the over-stoichiometric carbon-rich ($x \geq 1.5$) layers also contain segregated carbon with sp^2 and sp^3 hybridized bonding as shown in Fig. 1. Thus, we expect that the carbon content in the carbide phase does not match the carbon content of the overall films for $x \leq 0.24$ and $x \geq 1.5$. Consequently, we start our discussion with the $\text{TiC}_{0.5}$ and $\text{TiC}_{1.0}$ layers, which have measured relaxed lattice constants of $a_0 = 0.4305$ and 0.4325 nm, respectively. These values agree with reported experimental lattice constants (black open squares) of 0.4329 nm for $\text{TiC}_{0.94}$ [79], 0.4303–0.4316 nm for $\text{TiC}_{0.49-0.78}$ [10], 0.4312–0.4324 nm for $\text{TiC}_{0.6-0.8}$ [51], and 0.431 nm for $\text{TiC}_{1.0}$ [54]. They also agree quite well with our first-principles prediction of 0.4318 and 0.4299 nm for ordered Ti_2C and disordered $\text{TiC}_{0.5}$ and 0.4334 nm for stoichiometric TiC. The measured increase in the lattice constant between $x = 0.5$ and 1.0 is $da_0/dx = 0.004$ nm, which is in good agreement with the predicted slope of $da_0/dx = 0.003$ or 0.007 nm, depending on if using the ordered or disordered structure for $x = 0.5$. Previous theoretical studies have predicted similar slopes of $da_0/dx = 0.004$ nm [84] and 0.012 nm [85] using the local density approximation, as well as 0.009 nm [86] using the GGA.

Our measured a_0 for the TiC_{1.5} and TiC_{1.8} layers are 0.19 and 0.31% larger than for TiC_{1.0}, indicating that the lattice constant continues to increase with increasing C content for overstoichiometric TiC_x. However, the measured slope $da_0/dx = 0.002$ nm is quite small in comparison to the first principles predictions of most configurations plotted as navy lines in Fig. 6. This suggests that a large fraction of excess C does not incorporate into TiC as interstitial C or C-clusters but forms segregated graphitic or amorphous C. This is in agreement with our XPS and Raman analyses and is attributed to the large formation energies for single C interstitials (3.891 eV), Ti vacancies (6.845 eV), and C-clusters with energies per excess C atom > 1.5 eV for all investigated configurations, as discussed above and consistent with a recent study on the vacancy diffusion in TiC [87]. More specifically, using for example the predicted $da_0/dx = 0.039$ nm for C interstitials, the measured increase in a_0 between the TiC_{1.0} and TiC_{1.5} layers can be explained by a C interstitial concentration of only 2.3% per formula unit, corresponding to an $x = 1.023$. That is, the measured lattice constant of the TiC_{1.5} layer suggests a rocksalt-structure TiC_x phase with $x = 1.023$, while the remaining 32% C which corresponds to nearly all the excess carbon, forms a segregated phase that does not affect the measured a_0 . In the same manner, one could argue that the “8/4” C-defect structure with a predicted da_0/dx that nearly matches the experimental slope could equally well explain the measured a_0 , or alternatively a mixture of carbon pairs and triplets on cation sites, labeled as “2/1” and “3/1” in Fig. 6 could explain the measured a_0 . However, the large formation energy of these defect structures in combination with the coincidental compensation of positive and negative da_0/dx makes this explanation unlikely. Thus, the measured a_0 for overstoichiometric samples indicates, in combination with the predicted lattice constants, that the majority of the excess C forms segregated phases that do not affect the TiC lattice.

The positive measured da_0/dx also extends to the compositions with low carbon content, more specifically to the TiC_{0.24} layer which also contains an hcp Ti phase, as detected by XRD. The measured $da_0/dx = 0.004$ nm between $x = 0.24$ and 0.5 is identical (within experimental uncertainty) to the slope between $x = 0.5$ and 1.0, suggesting a continuous trend between $x = 0.24$ and 1.0 which could be attributed to an increasing C-vacancy concentration with decreasing x . However, the slope between $x = 0.25$ and 0.5 from first-principles calculations is seven times steeper than the measured value, in agreement with previously reported computational studies [84–86] and as evident from the plotted lattice constant for TiC_{0.25} which is well below the measured value for the TiC_{0.24} sample. Correspondingly, we estimate the composition of the TiC_x phase within the TiC_{0.24} layer using the first-principles calculated a_0 and find $x = 0.46$, which is exactly twice the carbon concentration of the overall layer. This estimate suggests that approximately half of this layer consists of the hcp Ti phase which, as discussed when presenting results in Fig. 5, contains only a small concentration of interstitial carbon. Interestingly, decreasing the experimental C concentration further causes an increase in a_0 , as the measured lattice constant for the TiC_{0.08} layer nearly matches that for TiC_{0.5}. This non-monotonic a_0 vs x behavior may be attributed to epitaxial constraints that facilitate growth of the cubic TiC_x phase despite a low carbon content, leading also to a large strain in the TiC_{0.24} sample, as presented in Fig. 4. In contrast, the TiC_{0.08} layer is fully relaxed, which we attribute to the dominance of the hexagonal phase in this layer. In fact, assuming a cubic TiC_{0.5} composition for this layer suggests that $\geq 84\%$ of the TiC_{0.08} layer exhibits the hexagonal phase, which makes it somewhat surprising that the cubic phase in this layer remains epitaxial as shown in Fig. 3.

Fig. 7 summarizes the results from nanoindentation measurements on TiC_x layers with $x = 0.08$ –1.8. The plot in Fig. 7(a) shows six typical loading and unloading curves from a TiC_{0.5} film with

maximum displacements $h_m = 40, 60, 80, 100, 120,$ and 140 nm. The inset is a $10 \times 10 \mu\text{m}^2$ scanning probe micrograph from the surface area where these six indents were performed. It shows a relatively smooth film surface with a root mean square roughness of 7 nm and large terraces that are 1–5 μm wide and are separated by discrete steps. The indents appear as triangular depressions which increase in width with increasing h_m , reaching a measured triangle side of 1.0 μm for $h_m = 140$ nm, in good agreement with the expected 1.0 μm width for a Berkovich tip with a 65° half-angle. The loading curves in Fig. 7(a) indicate minor pop-in events which occur near 40 nm for all indents except the $h_m = 40$ nm curve. They are attributed to the activation of the primary slip system in the titanium carbide crystal [88]. The hardness H is obtained from the measured maximum load and the projected contact area which is determined from h_m as described in Section 2. The plotted six curves yield $H = 24.9, 22.2, 23.7, 20.9, 22.1$ and 22.1 GPa for $h_m = 40$ –140 nm, suggesting that the hardness is independent of indentation depth within experimental uncertainty. This is shown in more detail in Fig. 7(b) which is a plot of the measured hardness as a function of contact depth h_c for three typical samples, namely the TiC_{0.08}, TiC_{1.0} and TiC_{1.5} layers. The data for this plot is obtained by performing 36 indents for each sample, with the maximum displacement ranging from $h_m = 10$ –120 nm, yielding h_c values ranging from 11 to 93 nm while outlier datapoints with $h_c < 10$ nm are excluded as described in Section 2. The measured $H = 8.7 \pm 1.1, 31.2 \pm 1.5,$ and 16.7 ± 1.3 GPa for TiC_{0.08}, TiC_{1.0} and TiC_{1.5}, respectively. These values are independent of h_c , validating the measured H and E values, as presented in Fig. 7(c, d).

Fig. 7(c) and (d) are plots of the hardness H and elastic modulus E vs the C-to-Ti ratio x in TiC_x/MgO(001) layers. H increases slightly from 8.7 ± 1.1 GPa to 10.5 ± 2.3 GPa for $x = 0.08$ and 0.24, increases sharply to 23.9 ± 1.4 and 31.2 ± 1.5 GPa for the TiC_{0.5} and TiC_{1.0} layers, and decreases again to 16.7 ± 1.3 and 13.5 ± 1.0 GPa for the TiC_{1.5} and TiC_{1.8} layers. The elastic modulus exhibits a similar composition dependence, increasing from 143 ± 16 GPa to 195 ± 26 GPa for $x = 0.08$ and 0.24, rising to 304 ± 9 and 462 ± 22 GPa for the phase-pure epitaxial carbide layers with $x = 0.5$ and 1.0, and dropping to 274 ± 11 and 201 ± 8 GPa for TiC_{1.5} and TiC_{1.8}. That is, the layers which are phase pure rocksalt-structure TiC_x exhibit the highest hardness and modulus, while the smaller values at low and high carbon content are attributed to the inclusion of metallic hcp Ti grains for $x \leq 0.24$ and amorphous/graphitic C for $x \geq 1.5$. Both inclusions are expected to facilitate ductile deformation and to reduce the average interatomic bond stiffness. More specifically, the TiC_{0.08} and TiC_{0.24} layers consist of a mixture of cubic rocksalt TiC_x and hcp-Ti phases, with an estimated > 84% and ~50% volume fraction of the hexagonal phase based on the above lattice constant analyses. Extrapolating the measured elastic constants from the TiC_{0.08} and TiC_{0.24} layers to $x = 0$ yields $E = 117 \pm 21$ GPa, which is close to the reported $E = 103$ GPa for pure metallic Ti [89]. This suggests that our measured elastic modulus is well described by an effective medium average of the two phases. In contrast, the hardness of the TiC_{0.08} layer which consists primarily of the hcp Ti phase is three times higher than the reported $H = 2.4$ –3.6 GPa for pure Ti [90], indicating a dramatic hardness improvement which is attributed to suppression of dislocation glide by interstitial C in the hcp phase and possibly also strain fields associated with coherent inclusions of rocksalt TiC grains [91]. Increasing the overall carbon content from $x = 0.08$ to 0.24 causes only a modest increase from $H = 8.7$ to 10.5 GPa, despite that the volume fraction of the C-containing hcp-Ti phase is reduced from > 84% to ~50%. This suggests that the more ductile hcp phase dominates the plastic deformation process and that the 50% volume fraction of the hard cubic carbide phase only slightly reduces the ductility facilitated by the

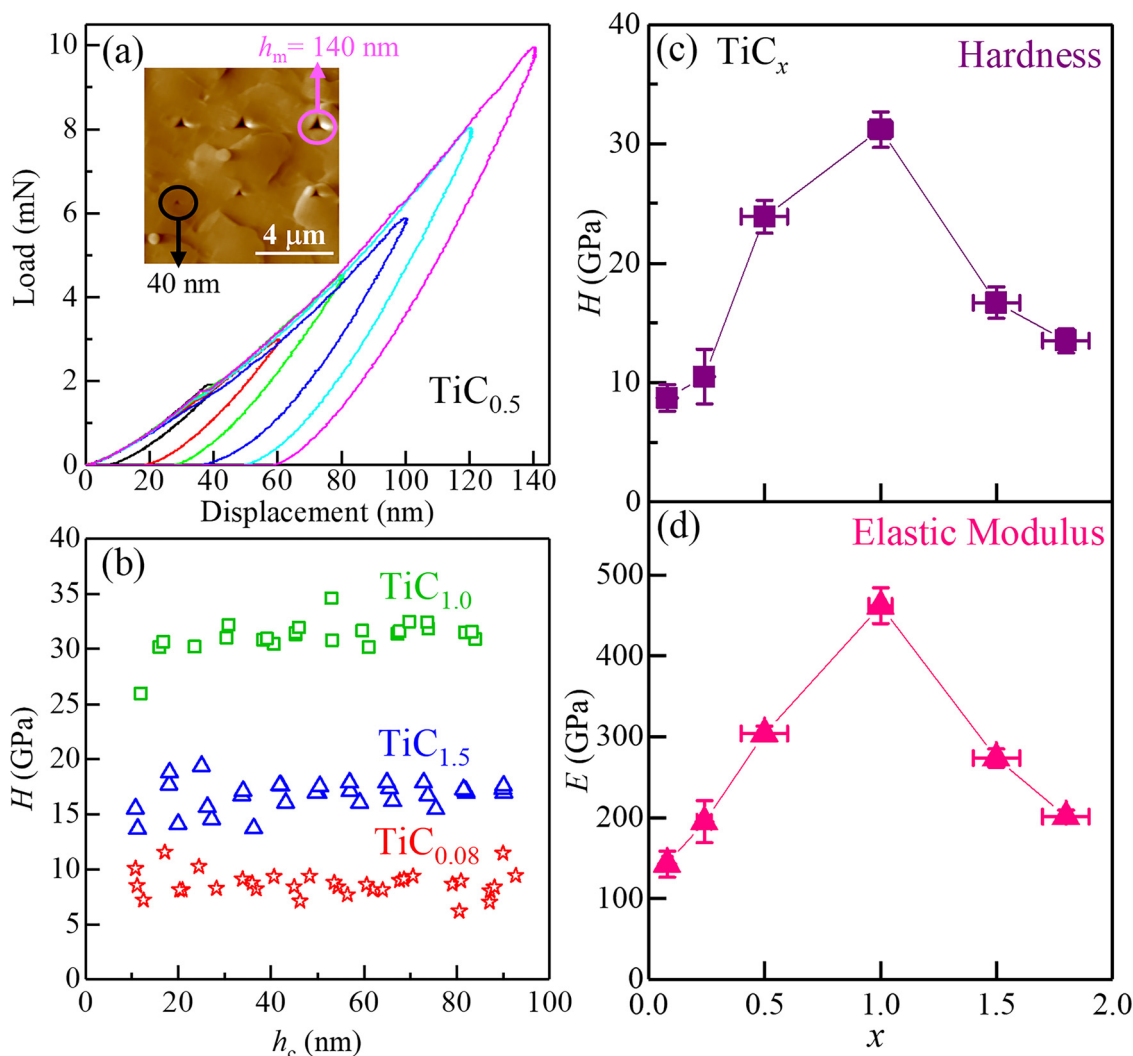


Fig. 7. (a) Nanoindentation load-displacement curves and *in situ* SPM topography map for maximum displacements $h_m = 40$ – 140 nm from an epitaxial $\text{TiC}_{0.5}(\text{001})$ film, (b) measured hardness H vs contact depth h_c for representative $\text{TiC}_{0.08}$ (red), $\text{TiC}_{1.0}$ (green) and $\text{TiC}_{1.5}$ (blue) films, (c) hardness H and (d) elastic modulus E as a function of the C-to-Ti ratio x in $\text{TiC}_x/\text{MgO}(\text{001})$ films.

hcp phase for $\text{TiC}_{0.24}$. We note when comparing the $x = 0.08$ and 0.24 samples that the former is fully relaxed while the latter has a strain of $\varepsilon_{\perp} = 0.5\%$, such that the modest hardness increase between $x = 0.08$ and 0.24 could also be attributed to compressive stress [92,93]. However, this hardness increase is of similar magnitude as the experimental uncertainty, suggesting that the strain effect is below our detection limit and can likely be neglected, especially for layers with $x \geq 0.5$ which have a considerably smaller strain, as discussed above.

The $\text{TiC}_{0.5}$ and $\text{TiC}_{1.0}$ layers are phase pure carbides, resulting in much higher hardnesses of 23.9 ± 1.4 and 31.2 ± 1.5 GPa than for the layers containing the secondary hcp phase. Conversely, Fig. 7(d) indicates that the elastic modulus increases (only) approximately linearly with x over the entire $0 < x < 1$ range, suggesting that a continuous transition from softer metallic Ti-Ti to stiffer ceramic (covalent/ionic) Ti-C bonds increases E without being affected by the relative phases within the layers. The measured values from the epitaxial $\text{TiC}_{0.5}(\text{001})$ and $\text{TiC}_{1.0}(\text{001})$ layers are in good agreement with previous reports, including $H = 30.1 \pm 1.6$ GPa and $E = 388 \pm 16$ GPa for epitaxial $\text{TiC}_{0.8}(\text{001})$ [94], $E = 437$ GPa from Ref. [95] and references therein, an increasing $H = 13, 24,$ and 35 GPa for nanocrystalline $\text{TiC}_{0.26}$, $\text{TiC}_{0.49}$, and $\text{TiC}_{0.78}$ layers [10] which agrees well despite the different microstructure, and

results from first-principles predictions with $H = 24$ – 32.5 GPa and $E = 431$ – 455 GPa for stoichiometric $\text{TiC}_{1.0}$ [64,95]. The measured increase in H and E can also be interpreted with the valence electron concentration VEC, which is used to describe the composition dependence of mechanical properties in rocksalt-structure nitrides [11,64]. More specifically, $\text{TiC}_{1.0}$ has a VEC = 8.0 and therefore nominally depleted d -orbitals that yield an expected high hardness and relatively brittle mechanical properties. In contrast, interpreting C vacancies as four-fold electron donors suggests that $\text{TiC}_{0.5}$ exhibits a considerable occupation of Ti d -orbitals and a VEC = 10.0, resulting in expected ductile properties with an approximately 20% lower E and a considerably reduced H in comparison to $\text{TiC}_{1.0}$. Our measured E and H qualitatively match these VEC arguments. However, we note that considerable p - d -hybridization in TiC may limit the validity of such arguments.

The decrease in H and E for increasing $x > 1$ is attributed to amorphous or graphitic C inclusions, similar to what has previously been reported for $\text{TiC}/\text{a-C}(\text{:H})$ [20,26,29]. More specifically, the $\text{TiC}_{1.5}$ and $\text{TiC}_{1.8}$ layers can be approximated as mixtures of a stoichiometric $\text{TiC}_{1.0}$ matrix and a-C inclusions where the volume fraction $V_{\text{a-C}} = 40 \pm 12$ and $51 \pm 11\%$, respectively, as determined from the XPS analyses. We estimate the elastic modulus of these mixtures using a constant stress approximation and $E = 462$ GPa

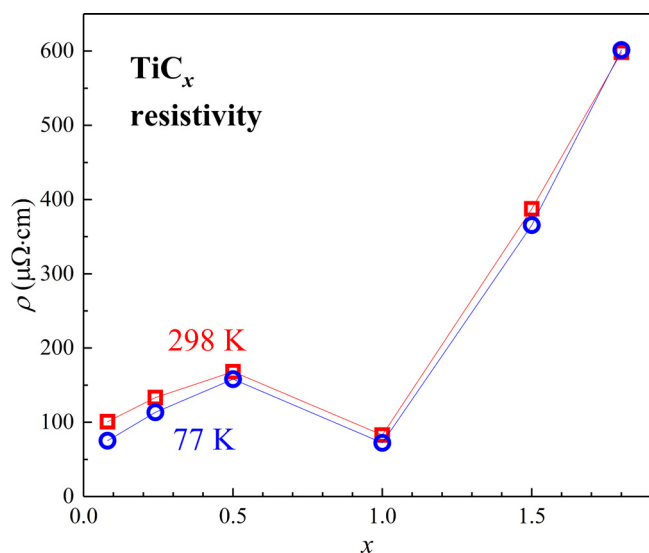


Fig. 8. Resistivity ρ vs x in TiC_x layers measured at 298 (red) and 77 K (blue).

from the phase-pure $\text{TiC}_{1.0}$ layer and $E = 140$ GPa for the a-C phase from Ref. [96]. This yields $E = 240 \pm 40$ and 210 ± 30 GPa for $x = 1.5$ and 1.8 , respectively, in good agreement with our measured 274 and 201 GPa for the $\text{TiC}_{1.5}$ and $\text{TiC}_{1.8}$ layers, suggesting that the elastic modulus is well described by a weighted average of the two phases.

Fig. 8 is a plot of the resistivity ρ vs carbon content x in TiC_x layers measured at room temperature (red) and at 77 K (blue). The room temperature resistivity increases nearly linearly from 101 to 133 to 168 $\mu\Omega\text{-cm}$ for $\text{TiC}_{0.08}$, $\text{TiC}_{0.24}$, $\text{TiC}_{0.5}$, respectively, drops to a minimum of 83 $\mu\Omega\text{-cm}$ for $x = 1.0$, and increases steeply to 388 and 598 $\mu\Omega\text{-cm}$ for $\text{TiC}_{1.5}$ and $\text{TiC}_{1.8}$. The relatively low resistivity for $x = 0.08$ is attributed to this layer primarily consisting of the hcp-Ti phase. However, its resistivity is more than twice the reported 42 $\mu\Omega\text{-cm}$ for pure hcp Ti at 298 K [97], indicating considerable electron scattering at crystalline defects (particularly carbon interstitials, consistent with the convex hull discussion presented in Fig. 5) which dominate over scattering at phonons. The measured resistivity decreases to $\rho_{77\text{K}} = 75$ $\mu\Omega\text{-cm}$ when reducing the temperature to 77 K, confirming metallic conduction. This decrease is comparable in magnitude to the reported $\Delta\rho = 36$ $\mu\Omega\text{-cm}$ decrease from 42 to 6.00 $\mu\Omega\text{-cm}$ of pure hcp Ti [97], suggesting that the $\text{TiC}_{0.08}$ sample primarily consists of hcp Ti, in perfect agreement with the lattice constant analysis. Increasing the carbon content to $x = 0.24$ and 0.5 results in a resistivity increase which is attributed to an increasing volume fraction of a more resistive $\text{TiC}_{0.5}$ phase (~50% and 100%, respectively) in these layers. We note that $\Delta\rho$ decreases to 19 and 10 $\mu\Omega\text{-cm}$, which may be attributed to weak carrier localization in the rocksalt-phase carbide, similar to what has previously been reported for rocksalt-structure transition metal nitrides with (1) eight valence electrons per formula unit including ScN [98], $\text{Sc}_{1-x}\text{Al}_x\text{N}$ [36], and $\text{Ti}_{1-x}\text{Mg}_x\text{N}$ [99], and (2) weak localization due to random arrangement of nitrogen vacancies in TaN_x [43,100], NbN_x [34], and HfN_x [39]. We note, however, that all our TiC_x layers have positive temperature coefficients of resistivity and are therefore “more metallic” than the above listed nitrides. The stoichiometric phase-pure $\text{TiC}_{1.0}$ layer has a similarly small positive $\Delta\rho = 11$ $\mu\Omega\text{-cm}$. However, its measured $\rho_{298\text{K}} = 83$ $\mu\Omega\text{-cm}$ is two times smaller than for the $\text{TiC}_{0.5}$ layer, suggesting that the latter contains a considerable density of electron scattering centers, indicating random anion site occupation. In contrast, randomness is minimized for the $\text{TiC}_{1.0}$ layer, resulting in a relatively low resistivity that is two-to-

four times smaller than previously reported room-temperature values of 130 $\mu\Omega\text{-cm}$ for $\text{TiC}_{0.95}$ [101], 110 $\mu\Omega\text{-cm}$ [49], 372 $\mu\Omega\text{-cm}$ [57], 260 $\mu\Omega\text{-cm}$ [15], 200 $\mu\Omega\text{-cm}$ for $\text{TiC}_{0.8}$ [51], 160 $\mu\Omega\text{-cm}$ for $\text{TiC}_{0.9-1.0}$ [54], 154–289 $\mu\Omega\text{-cm}$ [52] and 130–153 $\mu\Omega\text{-cm}$ for near-stoichiometric TiC [55]. This suggests that the $\text{TiC}_{1.0}(001)$ layer in our study has a lower defect concentration than those from previous reports. We attribute the low defect concentration to both epitaxial growth which minimizes grain boundary scattering and the relatively high growth temperature of 1100 °C which limits point defects caused by kinetic barriers for C diffusion. However, we note that $\rho_{77\text{K}}$ even for this layer is only 13% below that of $\rho_{298\text{K}}$, indicating that the majority of electron scattering is caused by residual point defects or, alternatively, random anion vacancies cause weak carrier localization. We also note that our measured $\rho_{298\text{K}} = 83$ $\mu\Omega\text{-cm}$ is larger than an extrapolated prediction of 56 $\mu\Omega\text{-cm}$ based on a measured ρ vs x [101]. The measured high resistivity for $x = 1.5$ and 1.8 is attributed to an increasing volume fraction of resistive amorphous or graphitic C with increasing x . The resistivity difference between 298 and 77 K remains small, with a measured $\Delta\rho = 22$ and -4 $\mu\Omega\text{-cm}$, respectively, suggesting metallic conduction with possible weak carrier localization for the $\text{TiC}_{1.5}$ and $\text{TiC}_{1.8}$ layers. We note that the large resistance without more substantial carrier localization is not easily explained by phase separated metallic TiC plus insulating a-C. More specifically, if there is a well-developed current path through the entire sample within the TiC phase, the resistance should be clearly metallic and smaller, as previously reported for annealed phase-separated $\text{Ti}_{0.46}\text{Al}_{0.54}\text{N}$ [102]. Contrary, if the current needs to travel through insulating a-C, then the resistance should exhibit more pronounced carrier localization. These arguments suggest that the TiC and a-C phases are intermixed on a small length-scale such that the percolation path within the TiC phase is considerably (five-fold) elongated and/or a-C clusters are such finely dispersed within the TiC matrix that electron transport within the TiC exhibits considerable additional electron scattering at carbon-cluster defect structures.

4. Conclusions

A combination of epitaxial layer growth, microstructural characterization, first-principles simulations, and mechanical property and transport measurements are used to explore the phase formation and intrinsic properties of titanium carbide TiC_x as a function of the C-to-Ti ratio x . 1 μm -thick TiC_x layers with C-to-Ti ratios $x = 0.08$ – 1.8 are sputter-deposited onto $\text{MgO}(001)$ substrates in Ar/CH_4 gas mixtures at 1100 °C by varying the methane gas fraction f_{CH_4} from 0.4% to 8%. Rocksalt-structure titanium carbide exhibits a cube-on-cube epitaxial relationship $(001)_{\text{TiC}} \parallel (001)_{\text{MgO}}$ and $[100]_{\text{TiC}} \parallel [100]_{\text{MgO}}$ for all layers with $x = 0.08$ – 1.5 . However, while $x = 0.5$ – 1.0 results in phase-pure carbides, layers with $x \leq 0.24$ contain hexagonal Ti and layers with $x \geq 1.5$ incorporate a-C with both sp^2 and sp^3 hybridized bonding. The measured relaxed lattice constant a_0 increases with x from 0.4304 nm for $\text{TiC}_{0.5}$ to 0.4325 nm for $\text{TiC}_{1.0}$, and continues to increase for $x > 1$. However, the latter increase is much smaller than predicted for C interstitials in TiC using density functional calculations, indicating that the majority of excess C incorporates into segregated a-C which does not affect the lattice constant of the carbide phase. This is consistent with large formation energies of C interstitials and C-clusters, rendering these configurations unlikely in cubic TiC. The calculated zero-temperature convex hull suggests phase separation into hcp Ti and ordered cubic Ti_2C for $0 < x < 0.5$. However, the configurational entropy increases the stability of random structures, resulting in an estimated $x = 0.063$ carbon solubility in hexagonal Ti at 1100 °C and possible cubic TiC_x with $x < 0.5$. These predictions are confirmed by experiments which indicate phase separation into cubic and hexagonal structures for $\text{TiC}_{0.08}$

and $\text{TiC}_{0.24}$, a hexagonal TiC_x phase with $x = 0.065$ and a cubic phase with $x = 0.46$. The measured hardness $H = 24$ and 31 GPa for phase-pure epitaxial $\text{TiC}_{0.5}(001)$ and $\text{TiC}_{1.0}(001)$ layers, respectively, and drops rapidly with the presence of secondary hcp Ti or a-C phases for $x < 0.5$ and $x > 1.0$. The elastic modulus is highest (462 GPa) for stoichiometric $\text{TiC}_{1.0}(001)$. It decreases approximately linearly with decreasing $x < 1.0$, which is attributed to a gradual transition from Ti-C to Ti-Ti bonds. Similarly, E also decreases with increasing $x > 1$, which is well described by a weighted average of the moduli of the two constituent phases TiC and a-C. The room-temperature resistivity of TiC_x films reaches a minimum $\rho = 83 \mu\Omega \text{ cm}$ at $x = 1.0$. It decreases by only 6–25% when cooling to 77 K for all layers, indicating the dominance of electron defect scattering over the entire investigated composition range $x = 0.08$ – 1.8 .

Declaration of Competing Interest

The authors declare that they have no known competing financial interests or personal relationships that could have appeared to influence the work reported in this paper.

Acknowledgment

The authors acknowledge financial support by the National Science Foundation under Grant Nos. 1712752, 1629230, and 1629239.

References

- [1] L.E. Toth, Transition Metal Carbides and Nitrides, Academic, New York, NY, USA, 1971.
- [2] U. Jansson, E. Lewin, Sputter deposition of transition-metal carbide films – a critical review from a chemical perspective, *Thin Solid Films* 536 (2013) 1–24.
- [3] N.J. Szymanski, I. Khatri, J.G. Amar, D. Gall, S.V. Khare, Unconventional superconductivity in 3D rocksalt transition metal carbides, *J. Mater. Chem. C* 7 (40) (2019) 12619–12632.
- [4] T. Glechner, R. Hahn, T. Wojcik, D. Holec, S. Kolozsvári, H. Zaid, S. Kodambaka, P.H. Mayrhofer, H. Riedl, Assessment of ductile character in superhard Ta-C-N thin films, *Acta Mater.* 179 (2019) 17–25.
- [5] H. Lasfargues, T. Glechner, C.M. Koller, V. Paneta, D. Primetzhofer, S. Kolozsvári, D. Holec, H. Riedl, P.H. Mayrhofer, Non-reactively sputtered ultra-high temperature Hf-C and Ta-C coatings, *Surf. Coat. Technol.* 309 (2017) 436–444.
- [6] N. Koutná, A. Brenner, D. Holec, P.H. Mayrhofer, High-throughput first-principles search for ceramic superlattices with improved ductility and fracture resistance, *Acta Mater.* 206 (2021) 116615.
- [7] H. Riedl, T. Glechner, T. Wojcik, N. Koutná, S. Kolozsvári, V. Paneta, D. Holec, D. Primetzhofer, P.H. Mayrhofer, Influence of carbon deficiency on phase formation and thermal stability of super-hard TaCy thin films, *Scr. Mater.* 149 (2018) 150–154.
- [8] D. Edström, D.G. Sangiovanni, L. Hultman, I. Petrov, J.E. Greene, V. Chirita, Elastic properties and plastic deformation of TiC- and VC-based pseudobinary alloys, *Acta Mater.* 144 (2018) 376–385.
- [9] J. Ding, Y. Meng, S. Wen, Mechanical properties and fracture toughness of multilayer hard coatings using nanoindentation, *Thin Solid Films* 371 (1–2) (2000) 178–182.
- [10] M. Guemmaz, A. Mosser, L. Boudoukha, J. Grob, D. Raiser, J. Sens, Ion beam synthesis of non-stoichiometric titanium carbide: composition structure and nanoindentation studies, *Nucl. Instrum.* 111 (3–4) (1996) 263–270.
- [11] I. Khatri, N.J. Szymanski, B.B. Dumre, J.G. Amar, D. Gall, S.V. Khare, Correlating structure and orbital occupation with the stability and mechanical properties of 3D transition metal carbides, *J. Alloy. Compd.* 891 (2022) 161866.
- [12] A.A. Voevodin, M.A. Capano, S.J.P. Laube, M.S. Donley, J.S. Zabinski, Design of a Ti/TiC/DLC functionally gradient coating based on studies of structural transitions in Ti-C thin films, *Thin Solid Films* 298 (1) (1997) 107–115.
- [13] S.K. Lee, C.M. Zetterling, E. Danielsson, M. Östling, J.P. Palmquist, H. Högborg, U. Jansson, Electrical characterization of TiC ohmic contacts to aluminum ion implanted 4H-silicon carbide, *Appl. Phys. Lett.* 77 (10) (2000) 1478–1480.
- [14] J.P. Palmquist, U. Jansson, T. Seppänen, P.O.Å. Persson, J. Birch, L. Hultman, P. Isberg, Magnetron sputtered epitaxial single-phase Ti_3SiC_2 thin films, *Appl. Phys. Lett.* 81 (5) (2002) 835–837.
- [15] J. Emmerlich, H. Högborg, S. Sasvári, P.O. Persson, L. Hultman, J.P. Palmquist, U. Jansson, J.M. Molina-Aldareguia, Z. Zsigány, Growth of Ti_3SiC_2 thin films by elemental target magnetron sputtering, *J. Appl. Phys.* 96 (9) (2004) 4817–4826.
- [16] K. Kimura, K. Shoji, Y. Yamamoto, W. Norimatsu, M. Kusunoki, High-quality graphene on SiC(000-1) formed through an epitaxial TiC layer, *Phys. Rev. B* 87 (7) (2013).
- [17] J. Halim, M.R. Lukatskaya, K.M. Cook, J. Lu, C.R. Smith, L.Å. Näslund, S.J. May, L. Hultman, Y. Gogotsi, P. Eklund, M.W. Barsoum, Transparent conductive two-dimensional titanium carbide epitaxial thin films, *Chem. Mater.* 26 (7) (2014) 2374–2381.
- [18] J. Wang, W.Z. Li, B. Shi, J.B. Luo, Nanoindentation study on the mechanical properties of TiC/Mo multilayers, *Thin Solid Films* 366 (1–2) (2000) 117–120.
- [19] J.W. Murray, R.B. Cook, N. Senin, S.J. Algodi, A.T. Clare, Defect-free TiC/Si multi-layer electrical discharge coatings, *Mater. Des.* 155 (2018) 352–365.
- [20] W. Meng, R. Tittsworth, L. Rehn, Mechanical properties and microstructure of TiC/amorphous hydrocarbon nanocomposite coatings, *Thin Solid Films* 377 (2000) 222–232.
- [21] T.H. Fang, S.R. Jian, D.S. Chuu, Nanomechanical properties of TiC, TiN and TiCN thin films using scanning probe microscopy and nanoindentation, *Appl. Surf. Sci.* 228 (1–4) (2004) 365–372.
- [22] S. Zhang, X.L. Bui, J. Jiang, X. Li, Microstructure and tribological properties of magnetron sputtered nc-TiC/a-C nanocomposite, *Surf. Coat. Technol.* 198 (1–3) (2005) 206–211.
- [23] W. Sekkal, A. Zaoui, S. Schmauder, Nanoindentation study of the superlattice hardening effect at TiC(110)/NbC(110) interfaces, *Appl. Phys. Lett.* 86 (16) (2005).
- [24] Y.T. Pei, D. Galvan, J.T.M. De Hosson, C. Strondl, Advanced TiC/a-C:h nanocomposite coatings deposited by magnetron sputtering, *J. Eur. Ceram. Soc.* 26 (4–5) (2006) 565–570.
- [25] Y. Hu, L. Li, X. Cai, Q. Chen, P.K. Chu, Mechanical and tribological properties of TiC/amorphous hydrogenated carbon composite coatings fabricated by DC magnetron sputtering with and without sample bias, *Diam. Relat. Mater.* 16 (1) (2007) 181–186.
- [26] J. Musil, P. Novák, R. Čerstvý, Z. Soukup, Tribological and mechanical properties of nanocrystalline-TiC/a-C nanocomposite thin films, *J. Vac. Sci. Technol. A* 28 (2) (2010) 244–249.
- [27] Z. Fogarassy, N. Oláh, I. Cora, Z.E. Horváth, T. Csanádi, A. Sulyok, K. Balázs, The structural and mechanical characterization of TiC and TiC/Ti thin films grown by DC magnetron sputtering, *J. Eur. Ceram. Soc.* 38 (7) (2018) 2886–2892.
- [28] A. Mani, P. Aubert, F. Mercier, H. Khodja, C. Berthier, P. Houduy, Effects of residual stress on the mechanical and structural properties of TiC thin films grown by RF sputtering, *Surf. Coat. Technol.* 194 (2–3) (2005) 190–195.
- [29] Y.T. Pei, D. Galvan, J.T.M. De Hosson, Nanostructure and properties of TiC/a-C:h composite coatings, *Acta Mater.* 53 (17) (2005) 4505–4521.
- [30] M.E. McGahay, B. Wang, J. Shi, D. Gall, Band gap and electron transport in epitaxial cubic $\text{Cr}_{1-x}\text{Al}_x\text{N}(001)$, *Phys. Rev. B* 101 (20) (2020).
- [31] B. Wang, K. Aryana, J.T. Gaskins, P.E. Hopkins, S.V. Khare, D. Gall, Structural stabilization and piezoelectric enhancement in epitaxial $(\text{Ti}_{1-x}\text{Mg}_x)_{0.25}\text{Al}_{0.75}\text{N}(0001)$ layers, *Adv. Funct. Mater.* 30 (30) (2020) 2001915.
- [32] B. Wang, M. Zhang, V. Adhikari, P. Fang, S.V. Khare, D. Gall, Bandgap and strain engineering in epitaxial rocksalt structure $(\text{Ti}_{0.5}\text{Mg}_{0.5})_{1-x}\text{Al}_x\text{N}(001)$ semiconductors, *J. Mater. Chem. C* 8 (36) (2020) 12677–12688.
- [33] B.D. Ozsdolay, X. Shen, K. Balasubramanian, G. Scannell, L. Huang, M. Yamaguchi, D. Gall, Elastic constants of epitaxial cubic MoNx (001) layers, *Surf. Coat. Technol.* 325 (2017) 572–578.
- [34] K. Zhang, K. Balasubramanian, B.D. Ozsdolay, C.P. Mulligan, S.V. Khare, W.T. Zheng, D. Gall, Growth and mechanical properties of epitaxial NbN(001) films on MgO(001), *Surf. Coat. Technol.* 288 (2016) 105–114.
- [35] B.D. Ozsdolay, C.P. Mulligan, M. Guerette, L. Huang, D. Gall, Epitaxial growth and properties of cubic WN on MgO(001), MgO(111), and $\text{Al}_2\text{O}_3(0001)$, *Thin Solid Films* 590 (2015) 276–283.
- [36] R. Deng, P.Y. Zheng, D. Gall, Optical and electron transport properties of rock-salt $\text{Sc}_{1-x}\text{Al}_x\text{N}$, *J. Appl. Phys.* 118 (1) (2015) 015706.
- [37] K. Zhang, K. Balasubramanian, B.D. Ozsdolay, C.P. Mulligan, S.V. Khare, W.T. Zheng, D. Gall, Epitaxial NbC $_{1-x}$ (001) layers: growth, mechanical properties, and electrical resistivity, *Surf. Coat. Technol.* 277 (2015) 136–143.
- [38] K. Zhang, M. Wen, S. Wang, R.P. Deng, D. Gall, W.T. Zheng, Sputter deposited NbC $_x$ Ny films: effect of nitrogen content on structure and mechanical and tribological properties, *Surf. Coat. Technol.* 258 (2014) 746–753.
- [39] H.S. Seo, T.Y. Lee, I. Petrov, J.E. Greene, D. Gall, Epitaxial and polycrystalline HfNx ($0.8 \leq x \leq 1.5$) layers on MgO(001): film growth and physical properties, *J. Appl. Phys.* 97 (8) (2005) 083521.
- [40] H.S. Seo, T.Y. Lee, J.G. Wen, I. Petrov, J.E. Greene, D. Gall, Growth and physical properties of epitaxial HfN layers on MgO(001), *J. Appl. Phys.* 96 (1) (2004) 878–884.
- [41] C.S. Shin, D. Gall, N. Hellgren, J. Patscheider, I. Petrov, J.E. Greene, Vacancy hardening in single-crystal TiNx(001) layers, *J. Appl. Phys.* 93 (10) (2003) 6025–6028.
- [42] D. Gall, C.S. Shin, T. Spila, M. Odén, M.J.H. Senna, J.E. Greene, I. Petrov, Growth of single-crystal CrN on MgO(001): effects of low-energy ion-irradiation on surface morphological evolution and physical properties, *J. Appl. Phys.* 91 (6) (2002) 3589–3597.
- [43] C.S. Shin, D. Gall, P. Desjardins, A. Vailionis, H. Kim, I. Petrov, J. Greene, M. Odén, Growth and physical properties of epitaxial metastable cubic TaN (001), *Appl. Phys. Lett.* 75 (24) (1999) 3808–3810.
- [44] D. Gall, I. Petrov, N. Hellgren, L. Hultman, J.E. Sundgren, J.E. Greene, Growth of poly- and single-crystal ScN on MgO(001): role of low-energy N_2^+ irradiation in determining texture, microstructure evolution, and mechanical properties, *J. Appl. Phys.* 84 (11) (1998) 6034–6041.

- [45] B.D. Ozsdolay, C.P. Mulligan, K. Balasubramanian, L. Huang, S.V. Khare, D. Gall, Cubic β -WN_x layers: growth and properties vs N-to-W ratio, *Surf. Coat. Technol.* 304 (2016) 98–107.
- [46] V. Lipatnikov, A. Rempel, A. Gusev, Atomic ordering and hardness of nonstoichiometric titanium carbide, *Int. J. Refract. Met. Hard Mater.* 15 (1–3) (1997) 61–64.
- [47] H. Okamoto, C-Ti (carbon-titanium), *J. Phase Equilib.* 19 (1998) 89–89.
- [48] J. Nickl, M. Reichle, Chemical vapor deposition in the titanium-carbon system, *J. Less Common. Met.* 24 (1) (1971) 63–72.
- [49] W.H. Sheu, S.T. Wu, Epitaxial growth of TiC(002) on Si(001) by reactive magnetron sputtering at low temperatures, *Jpn. J. Appl. Phys.* 37 (11R) (1998) 6094.
- [50] P. Eklund, H. Högborg, L. Hultman, Epitaxial TiC/SiC multilayers, *PSS (RRL)* 1 (3) (2007) 113–115.
- [51] L. Norin, S. McGinnis, U. Jansson, J.O. Carlsson, Low temperature deposition of epitaxial titanium carbide on MgO(001) by co-evaporation of C₆₀ and Ti, *J. Vac. Sci. Technol. A* 15 (6) (1997) 3082–3085.
- [52] N.C. Zaita, M. Dinu, A.E. Kiss, C. Logofatu, M. Braic, A comparative investigation of hetero-epitaxial TiC thin films deposited by magnetron sputtering using either hybrid DCMS/HiPIMS or reactive DCMS process, *Appl. Surf. Sci.* (2021) 537.
- [53] M. Braic, N.C. Zaita, M. Danila, C.E.A. Grigorescu, C. Logofatu, Hetero-epitaxial growth of TiC films on MgO(001) at 100°C by DC reactive magnetron sputtering, *Thin Solid Films* 589 (2015) 590–596.
- [54] N.C. Zaita, V. Braic, M. Danila, A.M. Vlaicu, C. Logofatu, C.E.A. Grigorescu, M. Braic, Influence of film thickness on the morphological and electrical properties of epitaxial TiC films deposited by reactive magnetron sputtering on MgO substrates, *J. Cryst. Growth* 389 (2014) 92–98.
- [55] Y.S. Fang, T.H. Do, K.A. Chiu, W.C. Chen, L. Chang, Reactive sputtering deposition of epitaxial TiC film on Si (100) substrate, *Coatings* 10 (7) (2020) 647.
- [56] M. Zhang, S. Kumar, R. Sundararaman, D. Gall, Resistivity scaling in epitaxial MAX-phase Ti₄SiC₃ (0001) layers, *J. Appl. Phys.* 130 (3) (2021) 034302.
- [57] G. Zou, H. Wang, N. Mara, H. Luo, N. Li, Z. Di, E. Bauer, Y. Wang, T. McCleskey, A. Burrell, Chemical solution deposition of epitaxial carbide films, *J. Am. Chem. Soc.* 132 (8) (2010) 2516–2517.
- [58] P. Fang, B. Wang, D. Gall, Epitaxial MoC_x: competition between cubic δ -MoC₁₁ and hexagonal β -Mo₂C (0001), *Surf. Coat. Technol.* 420 (2021) 127333.
- [59] P. Fang, B. Wang, C.P. Mulligan, T.M. Murray, S.V. Khare, D. Gall, Epitaxial growth of cubic WCy (001) on MgO (001), *J. Alloy. Compd.* 860 (2021) 158403.
- [60] C. Wagner, L. Davis, M. Zeller, J. Taylor, R. Raymond, L. Gale, Empirical atomic sensitivity factors for quantitative analysis by electron spectroscopy for chemical analysis, *Surf. Interface Anal.* 3 (5) (1981) 211–225.
- [61] W.C. Oliver, G.M. Pharr, An improved technique for determining hardness and elastic modulus using load and displacement sensing indentation experiments, *J. Mater. Res.* 7 (6) (1992) 1564–1583.
- [62] A.C. Fischer-Cripps, Critical review of analysis and interpretation of nanoindentation test data, *Surf. Coat. Technol.* 200 (14–15) (2006) 4153–4165.
- [63] G. Pharr, W. Oliver, Measurement of thin film mechanical properties using nanoindentation, *MRS Bull.* 17 (7) (1992) 28–33.
- [64] K. Balasubramanian, S.V. Khare, D. Gall, Valence electron concentration as an indicator for mechanical properties in rocksalt structure nitrides, carbides and carbonitrides, *Acta Mater.* 152 (2018) 175–185.
- [65] R. Chang, L.J. Graham, Low-temperature elastic properties of ZrC and TiC, *J. Appl. Phys.* 37 (10) (1966) 3778–3783.
- [66] F. Smits, Measurement of sheet resistivities with the four-point probe, *Bell Syst. Tech. J.* 37 (3) (1958) 711–718.
- [67] J.P. Perdew, K. Burke, M. Ernzerhof, Generalized gradient approximation made simple, *Phys. Rev. Lett.* 77 (18) (1996) 3865.
- [68] G. Kresse, D. Joubert, From ultrasoft pseudopotentials to the projector augmented-wave method, *Phys. Rev. B* 59 (3) (1999) 1758.
- [69] A. Zunger, S.H. Wei, L. Ferreira, J.E. Bernard, Special quasirandom structures, *Phys. Rev. Lett.* 65 (3) (1990) 353.
- [70] Z. Wang, S.M. Selbach, T. Grande, Van der Waals density functional study of the energetics of alkali metal intercalation in graphite, *RSC Adv.* 4 (8) (2014) 4069–4079.
- [71] H. Kang, Y. Matsuda, R. Shimizu, Preferential sputtering of TiC under keV Ar⁺ ion bombardment: simultaneous sputtering-ISS measurement with He⁺ and Ar⁺ ions, *Surf. Sci. Lett.* 134 (1) (1983) L500–L504.
- [72] E. Lewin, P.O.Å. Persson, M. Lattemann, M. Stüber, M. Gorgoi, A. Sandell, C. Ziebert, F. Schäfers, W. Braun, J. Halbritter, S. Ulrich, W. Eberhardt, L. Hultman, H. Siegbahn, S. Svensson, U. Jansson, On the origin of a third spectral component of C1s XPS-spectra for nc-TiC/a-C nanocomposite thin films, *Surf. Coat. Technol.* 202 (15) (2008) 3563–3570.
- [73] P. Merel, M. Tabbal, M. Chaker, S. Moisa, J. Margot, Direct evaluation of the sp³ content in diamond-like-carbon films by XPS, *Appl. Surf. Sci.* 136 (1–2) (1998) 105–110.
- [74] A.C. Ferrari, A. Libassi, B.K. Tanner, V. Stolojan, J. Yuan, L. Brown, S.E. Rodil, B. Kleinsorge, J. Robertson, Density, sp³ fraction, and cross-sectional structure of amorphous carbon films determined by X-ray reflectivity and electron energy-loss spectroscopy, *Phys. Rev. B* 62 (16) (2000) 11089.
- [75] A.C. Ferrari, J. Robertson, Interpretation of Raman spectra of disordered and amorphous carbon, *Phys. Rev. B* 61 (20) (2000) 14095–14107.
- [76] M.A. Durand, The coefficient of thermal expansion of magnesium oxide, *Physics* 7 (8) (1936) 297–298.
- [77] C. Houska, Thermal expansion and atomic vibration amplitudes for TiC, TiN, ZrC, ZrN, and pure tungsten, *J. Phys. Chem. Solids* 25 (4) (1964) 359–366.
- [78] P. Hidner, Thermal expansion of titanium, *J. Res. Natl. Bur. Stand* 30 (1943) (1934) 101.
- [79] A. Dunand, H. Flack, K. Yvon, Bonding study of TiC and TiN. I. High-precision x-ray-diffraction determination of the valence-electron density distribution, Debye-Waller temperature factors, and atomic static displacements in TiC_{0.94} and TiN_{0.99}, *Phys. Rev. B* 31 (4) (1985) 2299.
- [80] K. Balasubramanian, S.V. Khare, D. Gall, Energetics of point defects in rocksalt structure transition metal nitrides: thermodynamic reasons for deviations from stoichiometry, *Acta Mater.* 159 (2018) 77–88.
- [81] R. Bès, Y. Pipon, N. Millard-Pinard, S. Gavarini, M. Freyss, First-principles study of rare gas incorporation in titanium nitride, *Phys. Rev. B* 87 (2) (2013) 024104.
- [82] L. Raumann, D. Music, J.M. Schneider, Origin of the nitrogen over- and understoichiometry in Ti_{0.5}Al_{0.5}N thin films, *J. Phys. Condens. Matter* 24 (15) (2012) 155401.
- [83] Y. Lao, S. Hu, Y. Shi, Y. Deng, F. Wang, H. Du, H. Zhang, Y. Wang, Asymmetric interaction of point defects and heterophase interfaces in ZrN/TaN multilayered nanofilms, *Sci. Rep.* 7 (1) (2017) 1–9.
- [84] H.W. Hugosson, P. Korzhavyi, U. Jansson, B. Johansson, O. Eriksson, Phase stabilities and structural relaxations in substoichiometric TiC_{1-x}, *Phys. Rev. B* 63 (16) (2001).
- [85] Z. Dridi, B. Bouhafs, P. Ruterana, H. Aourag, First-principles calculations of vacancy effects on structural and electronic properties of TiCx and TiNx, *J. Phys. Condens. Matter* 14 (43) (2002) 10237.
- [86] M. Guemmaz, A. Mosser, R. Ahujab, B. Johansson, Elastic properties of substoichiometric titanium carbides: comparison of FP-LMTO calculations and experimental results, *Solid State Commun.* 110 (6) (1999) 299–303.
- [87] X. Tang, R. Salehin, G.B. Thompson, C.R. Weinberger, Statistical study of vacancy diffusion in TiC and TaC, *Phys. Rev. Mater.* 4 (9) (2020) 093602.
- [88] W. Mao, Y. Shen, C. Lu, Deformation behavior and mechanical properties of polycrystalline and single crystal alumina during nanoindentation, *Scr. Mater.* 65 (2) (2011) 127–130.
- [89] E. Fisher, C. Renken, Single-crystal elastic moduli and the hcp → bcc transformation in Ti, Zr, and Hf, *Phys. Rev.* 135 (2A) (1964) A482.
- [90] H. Attar, S. Ehtemam-Haghighi, D. Kent, I. Okulov, H. Wendrock, M. Bönisch, A. Volegov, M. Calin, J. Eckert, M. Dargusch, Nanoindentation and wear properties of Ti and Ti-TiB composite materials produced by selective laser melting, *Mater. Sci. Eng. A* 688 (2017) 20–26.
- [91] W.L. Finlay, J.A. Snyder, Effects of three interstitial solutes (nitrogen, oxygen, and carbon) on the mechanical properties of high-purity, alpha titanium, *JOM* 2 (2) (1950) 277–286.
- [92] S. Suresh, A. Giannakopoulos, A new method for estimating residual stresses by instrumented sharp indentation, *Acta Mater.* 46 (16) (1998) 5755–5767.
- [93] S. Carlsson, P.L. Larsson, On the determination of residual stress and strain fields by sharp indentation testing.: part II: experimental investigation, *Acta Mater.* 49 (12) (2001) 2193–2203.
- [94] H. Högborg, J. Birch, M. Odén, J. Malm, L. Hultman, U. Jansson, Growth, structure, and mechanical properties of transition metal carbide superlattices, *J. Mater. Res.* 16 (5) (2001) 1301–1310.
- [95] Y. Yang, H. Lu, C. Yu, J.M. Chen, First-principles calculations of mechanical properties of TiC and TiN, *J. Alloy. Compd.* 485 (1–2) (2009) 542–547.
- [96] B. Gupta, B. Bhushan, Micromechanical properties of amorphous carbon coatings deposited by different deposition techniques, *Thin Solid Films* 270 (1–2) (1995) 391–398.
- [97] T.G. Berlincourt, Hall effect, resistivity, and magnetoresistivity of Th, U, Zr, Ti, and Nb, *Phys. Rev.* 114 (4) (1959) 969.
- [98] R. Deng, B.D. Ozsdolay, P.Y. Zheng, S.V. Khare, D. Gall, Optical and transport measurement and first-principles determination of the ScN band gap, *Phys. Rev. B* 91 (4) (2015) 045104.
- [99] B. Wang, S. Kerdsonpanya, M.E. McGahay, E. Milosevic, P. Patsalas, D. Gall, Growth and properties of epitaxial Ti_{1-x}Mg_xN(001) layers, *J. Vac. Sci. Technol. A* 36 (6) (2018) 061501.
- [100] C.S. Shin, D. Gall, Y.W. Kim, P. Desjardins, I. Petrov, J. Greene, M. Odén, L. Hultman, Epitaxial NaCl structure δ -Ta₂N(001): electronic transport properties, elastic modulus, and hardness versus N/Ta ratio, *J. Appl. Phys.* 90 (6) (2001) 2879–2885.
- [101] S. Otani, T. Tanaka, Y. Ishizawa, Electrical resistivities in single crystals of TiCx and VCx, *J. Mater. Sci.* 21 (3) (1986) 1011–1014.
- [102] R. Rachbauer, J.J. Gengler, A.A. Voevodin, K. Resch, P.H. Mayrhofer, Temperature driven evolution of thermal, electrical, and optical properties of Ti–Al–N coatings, *Acta Mater.* 60 (5) (2012) 2091–2096.